UNIVERSITY OF CALIFORNIA

SANTA CRUZ

CHARACTERIZING CHLOROPHYLL IN THE GULF OF THE FARALLONES, CALIFORNIA, AND INVESTIGATING ITS RELATIONSHIP TO SURFACE CURRENTS, SEA SURFACE TEMPERATURE, AND THE SAN FRANCISCO BAY PLUME

A thesis submitted in partial satisfaction
of the requirements for the degree of

MASTER OF SCIENCE

in

OCEAN SCIENCES

by

Candice N. Cooper

September 2022

The Thesis of Candice Cooper
is approved:

_____
Professor Christopher A. Edwards, Chair

_____
Professor Raphael M. Kudela

_____
Professor John L. Largier

_____
Peter Biehl
Vice Provost and Dean of Graduate Studies

Table of Contents

1 INTRODUCTION 1

1.1 Overview of the California Current System 1

1.2 Study area 1

1.3 Gulf of the Farallones – Study motivation 2

1.4 Purpose 4

2 DATA 5

2.1 Chlorophyll 5

2.2 Surface currents 5

2.3 Sea surface temperature 5

2.4 SF Bay Plume 6

3 METHODS 7

3.1 Monthly climatology 7

3.2 Autocorrelation 7

3.3 EOF analysis 7

3.3.1 Univariate 7

3.3.2 EOF correlations 9

3.4 Plume analysis 9

4 RESULTS 11

4.1 Chlorophyll 11

4.1.1 PDFs 11

4.1.2 Autocorrelation 13

4.1.3 Monthly climatology & standard deviation 14

4.1.4 EOFs 16

4.1.5 Amplitude time series 19

4.1.6 Multivariate anecdotal descriptions 21

4.2 Surface currents 23
4.2.1 Monthly climatology 23
4.2.2 EOF 24
4.3 Sea surface temperature 26
4.3.1 Monthly climatology 26
4.3.2 EOF 27
4.4 EOF correlations 29
4.4.1 Chlorophyll & HFR 29
4.4.1.1 EOFs 29
4.4.1.2 Amplitude time series 33
4.4.2 Chlorophyll & SST 36
4.4.2.1 EOFs 36
4.4.2.2 Amplitude time series 39
4.4.3 Correlations 42
4.5 San Francisco Bay Plume 44
4.5.1 Monthly climatology 44
4.5.2 Plume vs. chlorophyll anomalies 45
5 DISCUSSION 46
5.1 Overview: Study area 46
5.2 Seasonal cycle 46
5.3 Interannual variability 48
5.4 Short term variability 50
5.5 Influence of the SF Bay Plume 52
5.6 Challenges 53
5.7 Conclusions 55
6 REFERENCES 57

List of Tables and Figures

Table 1. Pearson's r values and their associated p-values from EOF correlation analysis. All chlorophyll was log-transformed. Results with p-values < 0.05 are bolded. Correlations with r values ≥ |0.1| are highlighted in pink and correlations with r values ≥ |0.3| are highlighted in purple. 43

Figure 1. Map courtesy of Tezak et al. (2017). The Greater Farallones, Cordell Bank, and Monterey Bay National Marine Sanctuaries are outlined in white. The polygon encompassing the area of interest is outlined in black. Some labels have been added. 1

Figure 2. Example snapshot from June 26, 1998, of chlorophyll (mg/m^3) prior to the filling of missing pixels (left) and post-filling (right). This is an example of a frame that is close to the threshold. The 8-day OC-CCI chlorophyll product was used to produce this. The region within the pink polygon represents the area of interest. 8

Figure 3. Example of the smaller polygon used for plume analysis, outlined in purple. The daily MODIS Aqua nLw555 product was used to produce this figure of an April 29, 2017 snapshot. Contours represent where radiance is at 3, 5, 11, and 17 W m^{-2} μm^{-1} sr^{-1}. The thicker contour represents the plume threshold of 11 W m^{-2} μm^{-1} sr^{-1}. 10

Figure 4. Histogram of the probability density of linear chlorophyll (mg/m^3) within the area of interest, calculated using the daily OC-CCI chlorophyll product (1997-2021). A Gamma distribution curve is overlain on the figure, and was calculated using Equation 1. Values for the PDF parameters α and β are also printed on the figure. 12

Figure 5. Histogram of the probability density of log$_{10}$chlorophyll (mg/m^3) within the area of interest, calculated using the daily OC-CCI chlorophyll product (1997-2021). A Gaussian distribution curve is overlain on the figure, and was calculated using Equation 2. Values for the PDF parameters μ and σ are also printed on the figure. 12

Figure 6. Daily chlorophyll (mg/m^3) anomaly within the area of interest (upper), autocorrelation (middle), and integral time scale (lower). The daily OC-CCI chlorophyll

product (1997-2021) was used to calculate this. The blue minor grid lines on the chlorophyll anomaly time series are located on the 15th day of each month. For the autocorrelation and integral time scale, one lag is one day. A black line at y = 0 is plotted on the anomaly time series and autocorrelation. The area within the pink lines in the autocorrelation denotes the region of 95% confidence. The critical value was 1.96. 13

Figure 7. Chlorophyll (mg/m^3) monthly climatology (above) and time series of the monthly mean within the area of interest (below). Monthly means were calculated using the OC-CCI daily chlorophyll product (1997-2021). Contours represent where chlorophyll concentrations are 1, 3, 5, and 10 mg/m^3. The thicker contour line is at 3 mg/m^3. Labeled color bars are beneath each subplot. The grey shaded region of the time series is 2 standard deviations above and below the mean, representing the 95% confidence interval. 0 mg/m^3 is denoted by the blue horizontal dashed line. 14

Figure 8. Chlorophyll (mg/m^3) monthly standard deviation (above) and time series of the monthly mean standard deviation (below). Monthly means were calculated using the OC-CCI daily chlorophyll product (1997-2021). Contours represent where chlorophyll concentrations are 1, 3, 5, and 10 mg/m^3. The thicker contour line is at 3 mg/m^3. Labeled color bars are beneath each subplot. 15

Figure 9. First 4 modes of the linear chlorophyll EOF. The eigenvectors at each pixel are plotted for each mode. In the title of each subplot is the mode and percent of variability and cumulative variability explained by that mode. A labeled color bar is to the right of each subplot. The trend and seasonal cycle were removed prior to calculating the EOF. 17

Figure 10. First 4 modes of the log-transformed chlorophyll EOF. The eigenvectors at each pixel are plotted for each mode. In the title of each subplot is the mode and percent of variability and cumulative variability explained by that mode. A labeled color bar is to the right of each subplot. The trend and seasonal cycle were removed prior to calculating the EOF.....18

Figure 11. Monthly mean amplitudes for modes 1-4 of the linear chlorophyll EOF. The grey shaded region represents the standard error. The mode, and percent of variability and cumulative variability explained by that mode, are in the title of each time series.....20

Figure 12. Monthly mean amplitudes for modes 1-4 of the log-transformed chlorophyll EOF. The grey shaded region represents the standard error. The mode, and percent of variability and cumulative variability explained by that mode, are in the title of each subplot. 20

Figure 13. Snapshots of 8-day chlorophyll (mg/m^3), 8-day HFR (m/s), and 8-day SST (°C) composites on dates which display differing patterns in chlorophyll within the area of interest (outlined in pink for chl and HFR, and light blue for SST). Labeled color bars are to the right of each subplot. The date, product, mean, maximum, and minimum within the polygon are written in the title of each subplot. Contours for chlorophyll are at 1, 3, 5, 7, and 10 mg/m^3. The thicker contour is at 3 mg/m^3. Contours for SST are at 10, 11, 12, 13, and 14°C. The white contours are at 10 and 11°C. 22

Figure 14. HFR surface current (m/s) monthly climatology. Monthly means were calculated using 25-hour averages of the hourly HFRNet product (2012-2022). Labeled color bars are beneath each subplot. 23

Figure 15. First 4 modes of the HFR EOF. The eigenvectors at each pixel are plotted for each mode. In the title of each subplot is the mode and percent of variability and cumulative variability explained by that mode. Arrows indicate the direction of flow, and the length of the arrows indicate the strength of flow relative to that subplot. Color is indicative of speed. This analysis was performed on 25-hour averaged data and the trend and seasonal cycle were removed prior to calculating the EOF.....24

Figure 16. Sea surface temperature (°C) monthly climatology. Monthly means were calculated using the 8-day NOAA MODIS Aqua product (2002-2022). Contours represent where SSTs are 10, 11, 12, 13, 14, 15, 16, 17, and 18°C. Labeled color bars are beneath each subplot. 26

Figure 17. First 4 modes of the SST EOF. The eigenvectors at each pixel are plotted for each mode. In the title of each subplot is the mode and percent of variability and cumulative variability explained by that mode. A labeled color bar is to the right of each subplot. The trend and seasonal cycle were both removed prior to calculating the EOF. 28

Figure 18. First 4 modes of the log-transformed chlorophyll EOF (upper) and first 4 modes of the HFR EOF (lower) used for correlation analysis. The eigenvectors at each pixel are plotted for each mode. Arrows indicate the direction of flow, and the length of the arrows indicate the strength of flow relative to the rest of the flow in that subplot. For the HFR EOF, color is indicative of speed. In the title of each subplot is the mode and percent of variability and cumulative variability explained by that mode. A labeled color bar is to the right of each subplot. The trend and seasonal cycle were removed prior to calculating each EOF.....31

Figure 19. Monthly mean amplitudes for modes 1-4 of the log-transformed chlorophyll EOF and HFR EOF calculated for correlation analysis. The grey shaded region represents the standard error. The mode, and percent of variability and cumulative variability explained by that mode, are in the title of each time series. 35

Figure 20. First 4 modes of the log-transformed chlorophyll EOF (upper) and first 4 modes of the SST EOF (lower) used for correlation analysis. The eigenvectors at each pixel are plotted for each mode. In the title of each subplot is the mode and percent of variability and cumulative variability explained by that mode. A labeled color bar is to the right of each subplot. The trend and seasonal cycle were removed prior to calculating each EOF. 38

Figure 21. Monthly mean amplitudes for modes 1-4 of the log-transformed chlorophyll EOF and SST EOF calculated for correlation analysis. The grey shaded region represents the standard error. The mode, and percent of variability and cumulative variability explained by that mode, are in the title of each time series. 41

Figure 22. Normalized water-leaving radiance at the 555 nm band (nLw555) monthly climatology with units of W m^{-2} μm^{-1} sr^{-1}. Monthly means were calculated using the daily MODIS Aqua nLw555 product (2002-2021). Contours represent where nLw555 is 3, 5, 11, and 17 W m^{-2} μm^{-1} sr^{-1}. The thick contour represents the plume threshold of 11 W m^{-2} μm^{-1} sr^{-1}. Labeled color bars are located beneath each subplot. 44

Figure 23. Scatter plots of the monthly (upper) and daily (lower) chlorophyll anomalies (mg/m^3) vs. nLw555 ≥ 11 W m^{-2} μm^{-1} sr^{-1}, defined as the San Francisco Bay Plume. A least squares regression line (or line of best fit) is overlain on each figure. The r value and p-value are displayed in the upper left side of each figure and a legend in their upper right. Chlorophyll anomalies were calculated using the daily OC-CCI product (1997-2021) and nLw555 was retrieved from the daily MODIS Aqua product (2002-2021). 45

Figure 24. Time series of the monthly chlorophyll (mg/m^3) anomaly (upper) and SST (°C) anomaly (lower) within the area of interest for the years 2012-2020. Each year is plotted using a different color corresponding to the legend shown in the upper right corner of the upper panel. The line y = 0 is displayed as a black dashed line. Chlorophyll anomalies were calculated using the daily OC-CCI product (1997-2021) and SST anomalies were calculated using the 8-day NOAA MODIS Aqua product (2002-2022). 49

Figure 25. Scatter plot of the monthly chlorophyll (mg/m^3) anomalies vs. the monthly SST (°C) anomalies within the area of interest from July 2002-December 2021. A least squares regression line (or line of best fit) is overlain on the figure. The r value and p-value are displayed in the upper right and above that is a legend. Chlorophyll anomalies were calculated using the daily OC-CCI product (1997-2021) and SST anomalies were calculated using the 8-day NOAA MODIS Aqua product (2002-2022). 50

Figure 26. Histograms of the frequency of frames included for each month in the chlorophyll EOFs (upper, green), HFR EOF (mid-left, blue), SST EOF (mid-right, orange), chlorophyll & HFR EOFs for correlation analysis (lower left, purple), and chlorophyll & SST EOFs for correlation analysis (lower right, purple).....54

Abstract

Characterizing chlorophyll in the Gulf of the Farallones, California, and investigating its relationship to surface currents, sea surface temperature, and the San Francisco Bay Plume

Candice N. Cooper

This thesis presents a descriptive analysis of chlorophyll, surface currents, and sea surface temperature within the Gulf of the Farallones, occupying regions of three NOAA National Marine Sanctuaries along the central California coast. The seasonal cycles of each are described from a 24-year chlorophyll-*a* record, 10-year record of surface currents, and 20-year SST record. EOF analysis of chlorophyll revealed four distinct modes of variability: a single-signed pattern, a north-south split, an onshore-offshore structure, and a three-way split in which the Gulf of the Farallones is opposite to the regions north, south, and seaward. Surface currents via HF Radar and SST are also characterized through EOF analysis, to ultimately investigate their relationship to chlorophyll. Both surface currents and SST are significantly correlated to said patterns in chlorophyll, with the strongest correlation being between the north-south split in chlorophyll and an alongshore current pattern. A 19-year time series of normalized water-leaving radiance at the 555 nm band (nLw555) is used to calculate and describe the seasonal cycle of the San Francisco Bay Plume, which is compared to that of chlorophyll. Monthly and daily anomalies in chlorophyll are both significantly positively correlated to the magnitude of the SF Bay plume. The ecological structure of the area of interest to this study is of considerable importance to understand, particularly in order to implement effective conservation and management strategies.

Acknowledgements

I want to give a very special thank you to Chris for providing me this opportunity and for being both an amazing advisor and teacher. Your kindness, encouragement, and eagerness to uncover more did not go unnoticed.

I also want to thank the other members of my committee.

John and Raphe, thank you both for your continued helpful input, expertise, and enthusiasm toward this research.

A special thank you to Piero for so kindly sharing his San Francisco Bay Plume data with me, and for meeting with me to both provide insight into the data and to discuss this research.

I am grateful for the funding provided by the San Francisco Estuary Institute (SFEI; Award #1270) that supported this work, and want to specifically thank David Senn for both his time and enthusiasm toward this research as well.

I couldn't possibly write acknowledgements without also thanking my parents and family. Mom and Dad, thank you both for your endless support and for always encouraging me to work hard, take breaks, and follow my passions. I am incredibly lucky.

1 Introduction

1.1 Overview of the California Current System

The California Current is a broad, relatively shallow, primarily equatorward flowing surface current that is part of a larger eastern boundary current system, located on the eastern side of the anticyclonic North Pacific gyre. Nearshore, an inshore, poleward flow is also often found, largest in the fall and winter. Below these surface currents is a subsurface poleward flow known as the California Undercurrent (CU) that is most intense along the continental slope. Mixing between these currents is caused by the formation of eddies along the coast (Lynn & Simpson, 1990). The California Current System (CCS) has been described as trizonal, consisting of an oceanic/offshore zone, a coastal/nearshore zone, and an intervening transition zone (Lynn & Simpson, 1987).

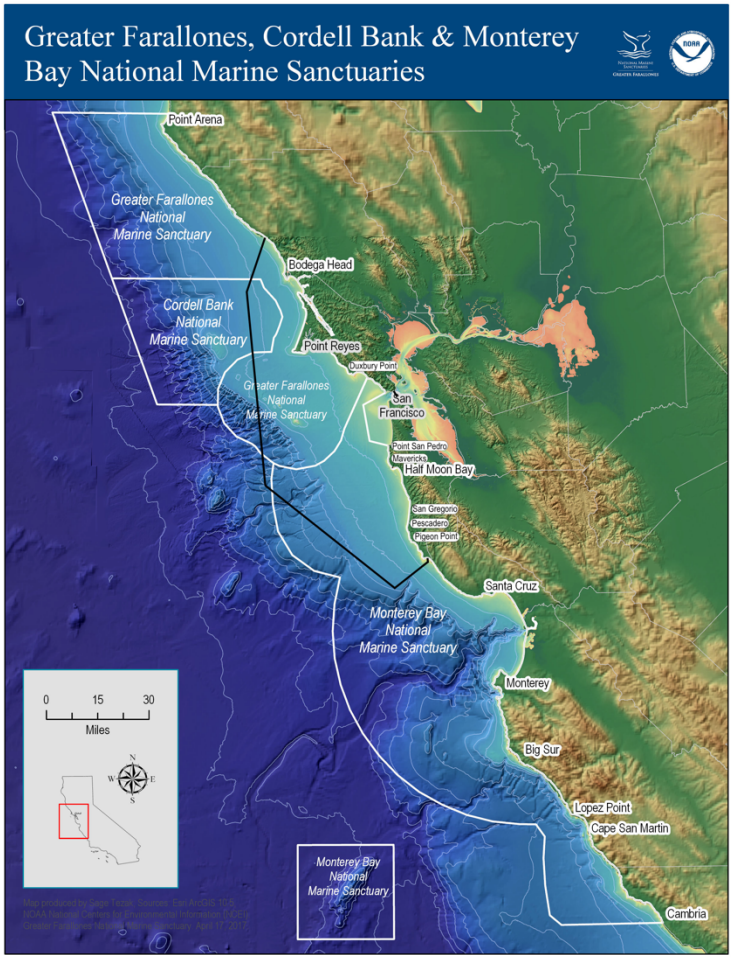

Figure 1. Map courtesy of Tezak et al. (2017). The Greater Farallones, Cordell Bank, and Monterey Bay National Marine Sanctuaries are outlined in white. The polygon encompassing the area of interest is outlined in black. Some labels have been added.

1.2 Study area

Located off the coast of central California, and centered about San Francisco Bay, the area of interest to this study encompasses portions of

three NOAA National Marine Sanctuaries, to include the Cordell Bank, Greater Farallones, and Monterey Bay National Marine Sanctuaries (NMS). The northern half of the study region is primarily within the Greater Farallones NMS, and the southern half is primarily within the Monterey Bay NMS (Fig. 1).

1.3 Gulf of the Farallones – Study motivation

As described by Chin et al. (1997), the Gulf of the Farallones encompasses the continental margin region extending west from shore at the Golden Gate to just inshore of the Farallon Islands at the shelf-slope break at 150 m depth. The area spans from the Point Reyes headland (38°N) at its northernmost point to west of Point San Pedro (37.6°N) at its southernmost point (Fig. 1).

Characterized by a wide shelf that slopes to the northwest, the complex bathymetry of the Gulf is quite unique when compared to the rest of the California coast (Chen et al., 1997; Steger et al., 1998; 2000; Yen et al., 2004). Local bathymetric features that can impact physical processes, such as surface currents, tides, internal waves, and eddies, have been found to influence the productivity and distribution of various marine fauna in this region and in others (Steger et al., 1998; Yen et al., 2004). The Gulf of the Farallones is an important breeding ground, migratory location, and sanctuary for numerous marine bird species and marine mammals (Yen et al., 2004). The Farallon Island Archipelago, located along the outer shelf directly seaward of the Gulf, is recognized by the U.S. Fish and Wildlife Service as a National Wildlife Refuge (NOAA, 2010; Yen et al., 2004). Together, the Gulf and Farallon Islands are responsible for the largest concentration of breeding marine birds in the contiguous United States, include one of the largest concentrations of adult white sharks in the world, and provide a destination feeding ground for endangered blue and humpback whales (NOAA, 2010).

San Francisco (SF) Bay waters likely influence waters in the Gulf of the Farallones, and

vice versa, due to exchange flow (Horner-Devine et al., 2015). Freshwater, sediments, pollutants (i.e., anthropogenic ammonium, plastics), nutrients (i.e., silicate), and plankton are transported by the SF Bay river plume into the Gulf and surrounding coastal ocean (Chappell et al., 2020). The Gulf is situated within the California Current System (CCS)—an active region of upwelling. Upwelling brings cool, nutrient-rich water to the ocean's surface, promoting biological productivity. Raimont & Cloern (2017) found that due to fast tidal oscillations inside SF Bay, the Central Bay responds relatively quickly—within less than a month—to oceanic temperature variability in the Gulf. Chlorophyll-*a*, on the other hand, did not have nearly as rapid a response, suggesting that patterns of coupling between the Gulf and SF Bay waters differs for physical/chemical mechanisms versus biological community interactions.

Placing this region in the broader context of other coastal embayments, specifically those connected to eastern boundary upwelling systems, there exist many similarities, as well as differences. It is common in these areas for a coastal upwelling jet to separate from the shoreline, subsequently impacting circulation into and out of nearby bays, estuaries, and lagoons (Bonicelli et al., 2014; Trautman & Walter, 2021). Based on the thermal structure and circulation patterns in and near Cartagena Bay, central Chile, for example, Bonicelli et al. (2014) found the region to be an important player in larval dispersal and material transport between the bay and nearby waters. Unlike in the Gulf of the Farallones, the continental shelf near Cartagena Bay is notably narrow (Bonicelli et al., 2014). Continental shelves support highly productive, intricate ecosystems (Kitchel et al, 2022); therefore, the previous statement concerning ecological importance may be even more applicable to the Gulf. Although also off the coast of central California, San Luis Obispo (SLO) Bay is much smaller and shallower than SF Bay, and thus exhibits fundamental differences in its dominant forcing mechanisms, including patterns of exchange flow (Trautman & Walter, 2021). Cartagena Bay and SLO Bay are both known as upwelling shadow systems because their topography prevents them from experiencing the same upwelling favorable winds as the surrounding coastal ocean, resulting

in retention zones that encourage the development of their own unique ecosystems (Trautman & Walter, 2021; Walter et al., 2018). Waters in the Ría de Vigo in northwest Spain, on the other hand, are driven by upwelling, downwelling, and the transitions between them, all on markedly short time scales of 2-4 days (Souto et al., 2003).

As a result of upwelled water being oxygen-poor, eastern boundary upwelling systems are commonly subject to hypoxic and anoxic conditions. St. Helena Bay off the coast of South Africa, for example, is known to experience seasonal hypoxia and episodic anoxia following the decay of red tides, both of which negatively impact local marine life (Pitcher et al., 2014). SF Bay has also experienced similar intervals of low oxygen, of which are sometimes also associated with harmful algal blooms (HABs), including red tides. However, unlike in St. Helena Bay, such occurrences are anomalous to SF Bay (Cloern et al., 2020). Other examples of coastal ocean influence on embayments include fluctuations in salinity within Willapa Bay, Washington, that—due to upwelling/downwelling—closely mimic fluctuations outside of the bay (Banas et al., 2004), the timing of the delivery of nutrients into Tillamook Bay estuary off the Oregon coast (Colbert & McManus, 2003), and the development of surface slicks following upwelling events near Monterey Bay, CA, ultimately influencing the ecology of plankton within the bay (Ryan et al., 2010).

1.4 Purpose

The main purpose of this paper is to characterize patterns of chlorophyll in the Gulf of the Farallones. Surface currents and sea surface temperature are also characterized to investigate their relationship to chlorophyll in the same region. The association between the chlorophyll signal in the Gulf and the San Francisco Bay Plume is also investigated. It is necessary to gain a better understanding of these patterns and the mechanisms they may be linked to in order to explain the ecological structure of this region and continue to implement effective conservation and management strategies in the future.

2 Data

2.1 Chlorophyll

Multi-sensor satellite-derived chlorophyll-*a* concentrations (referred to as chlorophyll throughout this paper) were obtained from Plymouth Marine Laboratory's (PML) Ocean Colour Climate Change Initiative dataset (OC-CCI; https://www.esa-oceancolour-cci.org), Version 5.0, operated by the European Space Agency (ESA). Daily and 8-day data products were downloaded with time series spanning from September 4, 1997–December 31, 2021, at spatial resolutions of 1 km and 4 km, respectively. For the 8-day product, the dates correspond to the beginning of the 8-day composite period. Due to substantial cloud cover present in the daily product (and the 5-day product), the 8-day product was better suited for some of our analyses. However, due to the higher resolution of the daily product, it was still utilized. The sensors merged to produce both data products were MERIS, MODIS Aqua, SeaWiFS LAC & GAC, VIIRS, and OLCI (Sathyendranath et al., 2019; 2021).

2.2 Surface currents

High frequency radar (HFR) data was provided by the U.S. Integrated Ocean Observing System's (IOOS) HFRadar Network (HFRNet), and was accessed through the Coastal Observing Research and Development Center (CORDC) at Scripps Institution of Oceanography (https://cordc.ucsd.edu/projects/mapping/). Hourly surface velocity data spanning from January 6, 2012–June 2, 2022 was obtained at a spatial resolution of 6 km. The instruments used to produce said dataset were Earth Remote Sensing Instruments, Active Remote Sensing, Profilers/Sounders, Radar Sounders, and Doppler RADAR (Terrill et al., 2006).

2.3 Sea surface temperature

Measurements of sea surface temperature (SST) were taken by the Moderate

Resolution Imaging Spectroradiometer (MODIS) from NASA's Aqua Spacecraft. We obtained these records of satellite-retrieved SST from the National Oceanic and Atmospheric Administration's (NOAA) CoastWatch West Coast Regional Node (https://www.pfeg.noaa.gov), processed by NASA's Goddard Space Flight Center (https://oceancolor.gsfc.nasa.gov). More specifically, the dataset was retrieved from the NOAA Environmental Research Division (ERD) at the Southwest Fisheries Science Center (SWFSC) run by the National Marine Fisheries Service (NMFS, otherwise known as NOAA fisheries) and National Environmental Satellite, Data, and Information Service (NESDIS). An 8-day SST composite was downloaded with time series spanning from July 5, 2002–March 25, 2022 at a spatial resolution of approximately 1.47 km from daytime satellite passes only. The dates correspond to the center of the 8-day composite period. Due to considerable cloud cover present in the daily and 3-day SST products, the 8-day product was better suited for our analyses. Relative to the chlorophyll and HFR products, the 8-day product in this case is at high resolution. All data was accessed through the NOAA ERDDAP server (Brown and Minnett, 1999).

2.4 SF Bay Plume

Otero & Siegel (2004) found normalized water-leaving radiance at the 555 nm band (nLw555) to be a good proxy for suspended sediment, and therefore, a good river plume indicator. A record of nLw555 was kindly provided to us by Professor Piero Mazzini at the Virginia Institute of Marine Science. Retrieved by the MODIS from NASA's Aqua Spacecraft, the time series of this daily data product spans from July 4, 2002–September 10, 2021. It was initially processed from L1 and L2 (with default L2 flags applied) using SeaDAS 8.1.0 (https://seadas.gsfc.nasa.gov) to a spatial resolution of 1 km, but was later interpolated by Piero to a spatial resolution of approximately 800 m. To adjust for atmospheric correction, the NIR-SWIR procedure for coastal turbid regions was applied following the methods in Wang et

al. (2009). All processing was performed by Cassia Pianca and Piero Mazzini. Their plume detection technique identified a radiance of 11 W m^{-2} μm^{-1} sr^{-1} as the threshold for San Francisco Bay Plume waters.

3 Methods

3.1 Monthly climatology

A monthly climatology was calculated from monthly averages of chlorophyll, HFR, SST, and nLw555. The daily chlorophyll and nLw555 products were used for this purpose. To filter out tidal influence on the HFR data, 25-hour averages were calculated prior to calculating its monthly mean (Yasui et al., 2022). For SST, monthly averages were calculated from the 8-day product.

3.2 Autocorrelation

An autocorrelation and integral time scale were determined for the daily anomalies in chlorophyll. To calculate the daily anomalies, a monthly average was calculated and stored as the 15th day of each month, and this information was linearly interpolated in time to each calendar day of the year. That multi-year daily average was then subtracted from the single daily average value. The critical value for a 95% confidence interval was calculated as $\sqrt{2}$ multiplied by the inverse error function of 0.95.

3.3 EOF analysis

3.3.1 Univariate

Empirical orthogonal function (EOF) analyses were performed on the 8-day chlorophyll (linear and log-transformed), 25-hour averaged HFR, and 8-day SST individually. EOF calculations require continuous time series, and therefore, additional data processing was necessary due to missing data points during periods of cloud cover.

A polygon was created to encompass the area of interest, and land points were omitted. We only processed data frames that exceeded a threshold fraction of valid ocean pixels, with the threshold depending on the dataset. An 80% threshold for both chlorophyll and SST was found to provide a good balance between having a manageable number of pixel omissions and a large overall time series. HFR coverage was considerably better and allowed a 99% threshold to be used. The scatteredInterpolant function within MATLAB was applied with the nearest neighbor method to fill the missing pixels in the remaining frames (MATLAB ver. R2021b). An example of this filling procedure for a near-threshold case is shown in Figure 2. For each dataset, both the trend and seasonal cycle were removed using the detrend3 and deseason functions from the Climate Data Toolbox for MATLAB (Greene et al., 2019). The eof function within the same toolbox was used to calculate the chlorophyll and SST EOFs. Since the surface velocity data is multivariate, comprising both a north-south and east-west component, it required us to modify the function (which is univariate) to allow for the HFR EOF calculation. The first 4 modes in each EOF were plotted and the modal amplitude seasonal cycle was calculated and plotted as time series for each mode in each EOF. Standard error was calculated as the monthly standard deviation—normalized by N-1—divided by N, where N is the sample size.

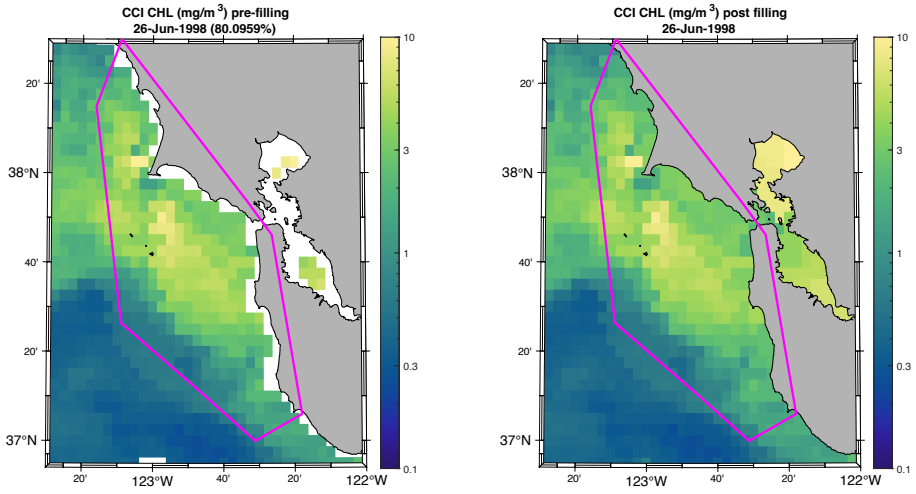

Figure 2. Example snapshot from June 26, 1998, of chlorophyll (mg/m^3) prior to the filling of missing pixels (left) and post-filling (right). This is an example of a frame that is close to the threshold. The 8-day OC-CCI chlorophyll product was used to produce this. The region within the pink polygon represents the area of interest.

3.3.2 EOF correlations

Additional EOF analyses were performed prior to any correlation analyses. An 8-day HFR composite was produced from the 25-hour averaged HFR. The dates of the 8-day chlorophyll product were matched with the dates of the newly compiled 8-day HFR product. The data was then processed using the same technique previously described. A threshold of 85% was used for chlorophyll and a threshold of 99% was used for HFR. Univariate EOF analyses were performed on chlorophyll and HFR with the remaining frames. Correlation coefficients and p-values were calculated between each of the first 4 modes of chlorophyll and HFR. Statistical significance was set at the 5% level. This process was repeated using the 8-day chlorophyll and 8-day SST products. A threshold of 80% was used for chlorophyll and a threshold of 75% was used for SST. It is important to note that because the date corresponds to the beginning of the 8-day period for the chlorophyll product used, but to the center of the 8-day period for the SST product, there is approximately a 3.5-day lag in chlorophyll. To correct for this, the dates were adjusted to reflect the same date compositing time period.

3.4 Plume analysis

Mean monthly and daily anomalies in chlorophyll were calculated and subsequently correlated with the mean normalized water-leaving radiance (W m^{-2} μm^{-1} sr^{-1}) at 555 nm at times when it either met or exceeded the SF Bay plume threshold of 11 W m^{-2} μm^{-1} sr^{-1}. Due to the spatial distribution of the plume, a smaller polygon was created to maintain a sufficient number of nLw data points that were ≥ the plume threshold for the correlation analysis. An example of this polygon can be seen in Figure 3. Monthly chlorophyll anomalies were calculated as the monthly mean for each year minus the monthly mean across all years. Daily anomalies in chlorophyll were calculated using the same method as was used for the autocorrelation analysis. Statistical significance was set at the 5% level.

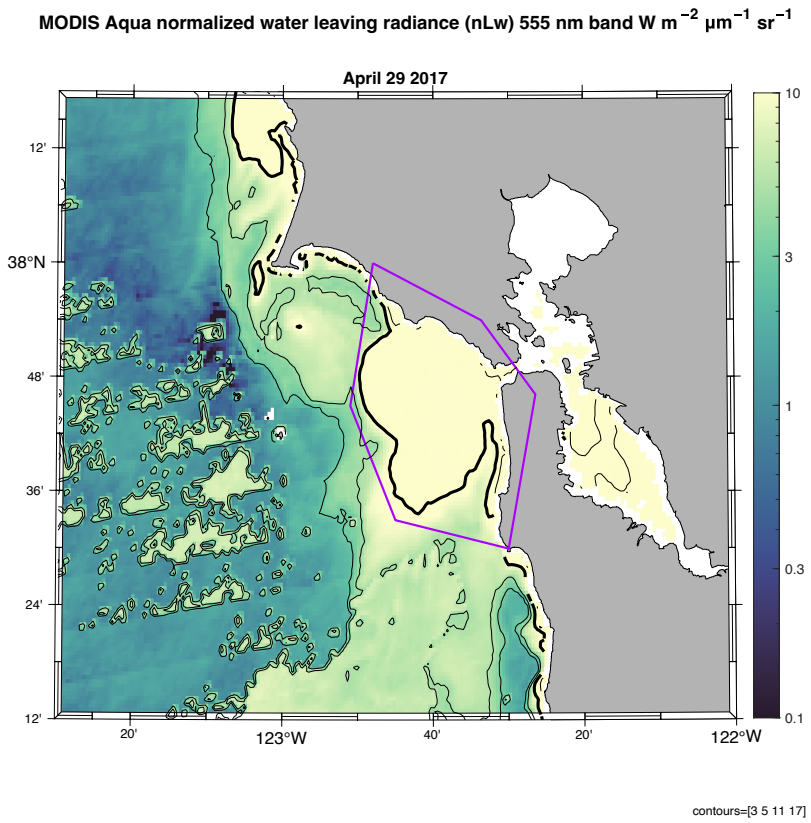

Figure 3. Example of the smaller polygon used for plume analysis, outlined in purple. The daily MODIS Aqua nLw555 product was used to produce this figure of an April 29, 2017 snapshot. Contours represent where radiance is at 3, 5, 11, and 17 W m^{-2} μm^{-1} sr^{-1}. The thicker contour represents the plume threshold of 11 W m^{-2} μm^{-1} sr^{-1}.

4 Results

4.1 Chlorophyll

4.1.1 PDFs

The mean daily chlorophyll within the area of interest was skewed to the right and fit a Gamma distribution (Fig. 4, Eq. 1). It had a maximum of 31.41 mg/m^3 and a minimum of 0.09 mg/m^3, however 99.34% of the data had a value between 0 and 10 mg/m^3 and 92.87% had a value between 0 and 5 mg/m^3. Its mean was 2.58 mg/m^3. The probability distribution function, or PDF, for a Gamma distribution is:

$$f(x) = \frac{(x/\beta)^{\alpha-1}\exp(-x/\beta)}{\beta\Gamma(\alpha)} \quad (\textbf{Equation 1})$$

where α is the shape parameter, β is the scale parameter, and $\Gamma(\alpha)$ is the gamma function.

The log-transformed chlorophyll, on the other hand, was approximately Gaussian, or normally distributed (Fig. 5, Eq. 2). Its maximum was 1.50 mg/m^3 and its minimum was -1.03 mg/m^3. Approximately 68.3% of the data fell within 0.06-0.60 mg/m^3, or 1 standard deviation of the mean. Approximately 95.5% of the data fell within -0.21-0.87 mg/m^3, or 2 standard deviations of the mean. Approximately 99.7% of the data fell within -0.48-1.14 mg/m^3, or 3 standard deviations of the mean. The PDF for a Gaussian distribution is:

$$f(x) = \frac{1}{\sigma\sqrt{2\pi}}\exp\left[-\frac{(x-\mu)^2}{2\sigma^2}\right] \quad (\textbf{Equation 2})$$

where μ is the mean and σ is the standard deviation.

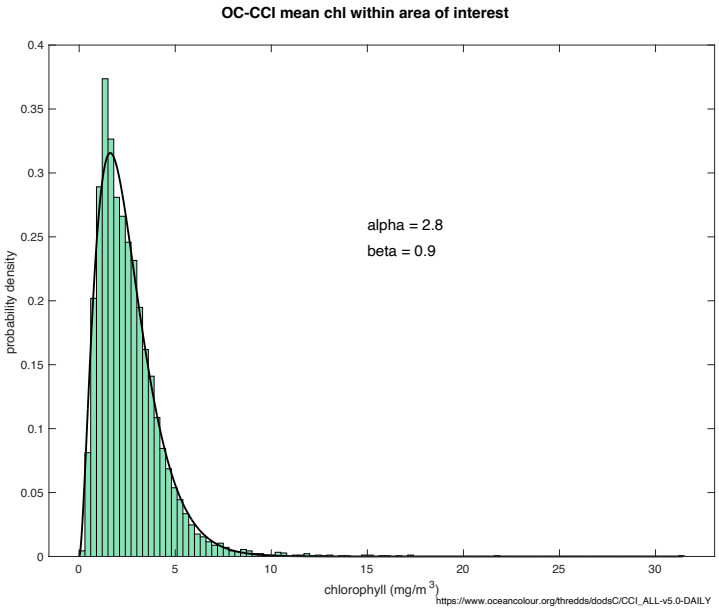

Figure 4. Histogram of the probability density of linear chlorophyll (mg/m^3) within the area of interest, calculated using the daily OC-CCI chlorophyll product (1997-2021). A Gamma distribution curve is overlain on the figure, and was calculated using Equation 1. Values for the PDF parameters α and β are also printed on the figure.

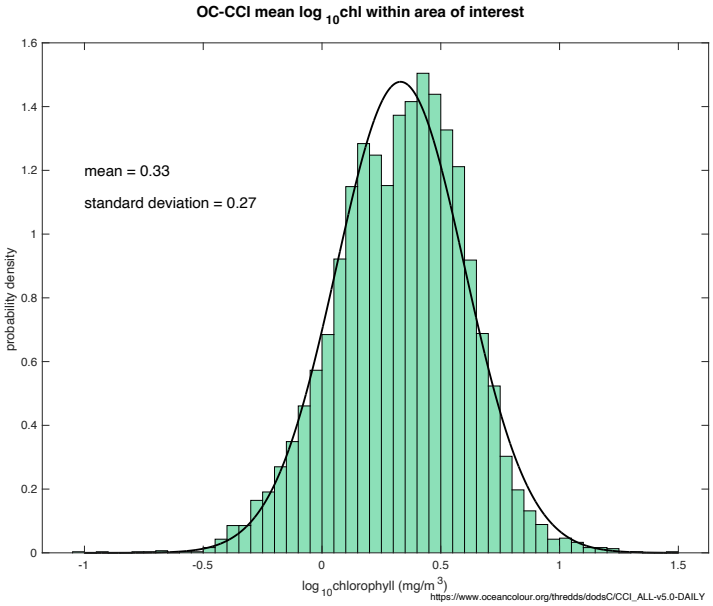

Figure 5. Histogram of the probability density of $\log_{10}$chlorophyll (mg/m^3) within the area of interest, calculated using the daily OC-CCI chlorophyll product (1997-2021). A Gaussian distribution curve is overlain on the figure, and was calculated using Equation 2. Values for the PDF parameters μ and σ are also printed on the figure.

4.1.2 Autocorrelation

The daily chlorophyll anomaly within the area of interest, its autocorrelation, and its integral time scale are shown in Figure 6. The autocorrelation drops rapidly in the first 10 days, first crosses the 95% confidence interval at 44 lags (days), and first crosses zero at 116 lags (days). The integral time scale for the daily chlorophyll anomaly indicates that on average chlorophyll in the Gulf of the Farallones is autocorrelated out to between 4 days and a week.

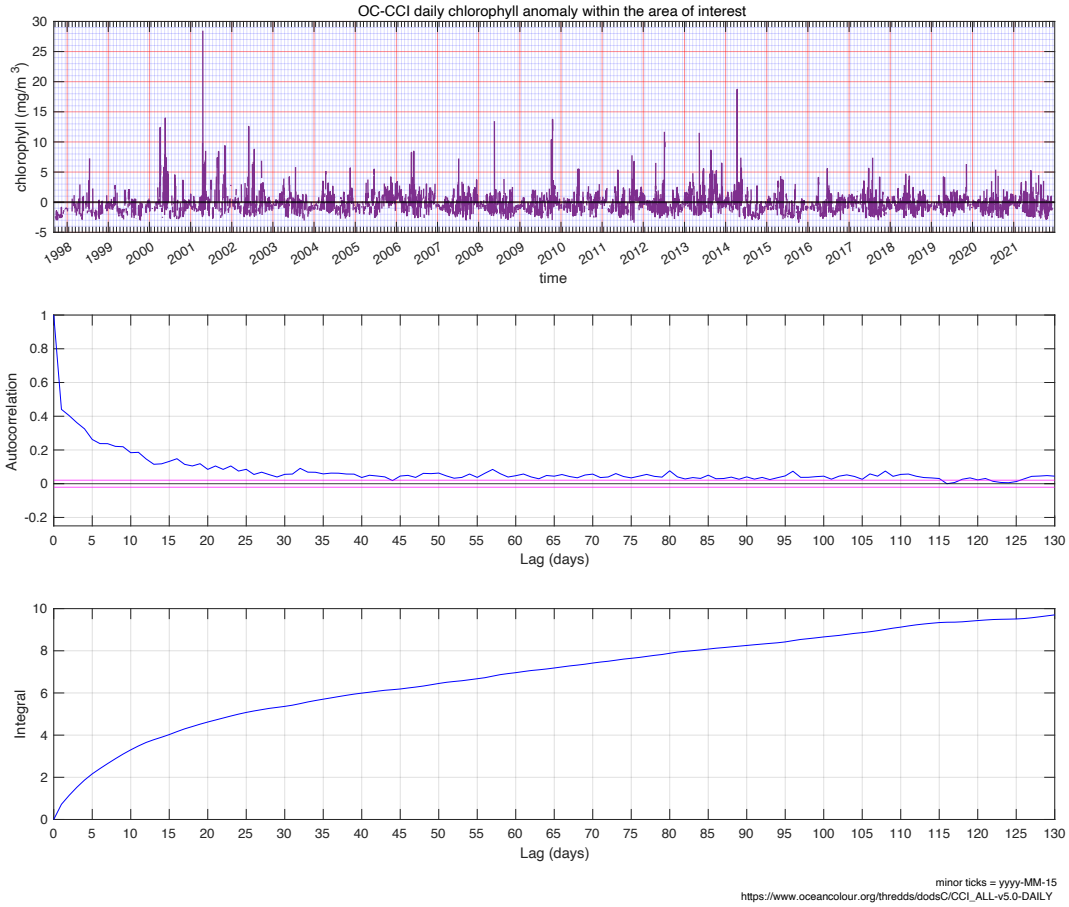

Figure 6. Daily chlorophyll (mg/m^3) anomaly within the area of interest (upper), autocorrelation (middle), and integral time scale (lower). The daily OC-CCI chlorophyll product (1997-2021) was used to calculate this. The blue minor grid lines on the chlorophyll anomaly time series are located on the 15th day of each month. For the autocorrelation and integral time scale, one lag is one day. A black line at y = 0 is plotted on the anomaly time series and autocorrelation. The area within the pink lines in the autocorrelation denotes the region of 95% confidence. The critical value was 1.96.

4.1.3 Monthly climatology & standard deviation

The monthly climatology and standard deviation of chlorophyll within the study domain are shown in Figures 7 and 8, respectively. Even though the linear chlorophyll is not represented by a Gaussian distribution, the standard deviation helps to give a scale of variability. Spatially, the chlorophyll signal outside the Golden Gate in the Gulf of the Farallones (37.5-38°N) is smallest in the winter months (December–February) when the mean gets as low as 1.85 mg/m^3, and largest in late spring through early summer (April–July), when the mean reaches a maximal concentration of 3.24

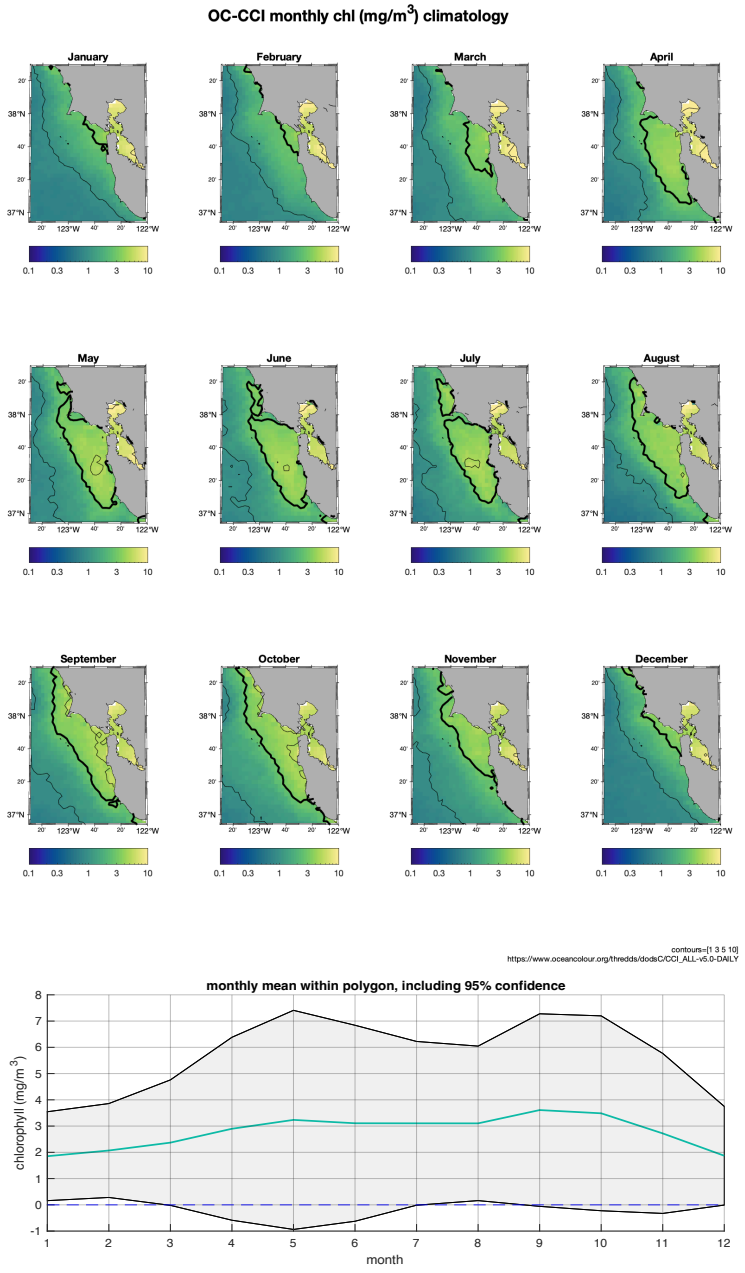

Figure 7. Chlorophyll (mg/m^3) monthly climatology (above) and time series of the monthly mean within the area of interest (below). Monthly means were calculated using the OC-CCI daily chlorophyll product (1997-2021). Contours represent where chlorophyll concentrations are 1, 3, 5, and 10 mg/m^3. The thicker contour line is at 3 mg/m^3. Labeled color bars are beneath each subplot. The grey shaded region of the time series is 2 standard deviations above and below the mean, representing the 95% confidence interval. 0 mg/m^3 is denoted by the blue horizontal dashed line.

mg/m^3 in May. Although spatially distributed tighter along the coast, the chlorophyll plume is still very much present in late summer and early fall (August–November), when mean chlorophyll concentrations sometimes reach their annual peak of 3.61 mg/m^3 in September. At the beginning of its springtime growth in March–April, highest chlorophyll values are found south of Pt. Reyes and extend southward to Año Nuevo Point (37.1°N). From August–November, high chlorophyll values connected to SF Bay are also present more northward past Pt. Reyes. Not only is the range of mean values within the Gulf relatively small, but anomalous months can look very different from what

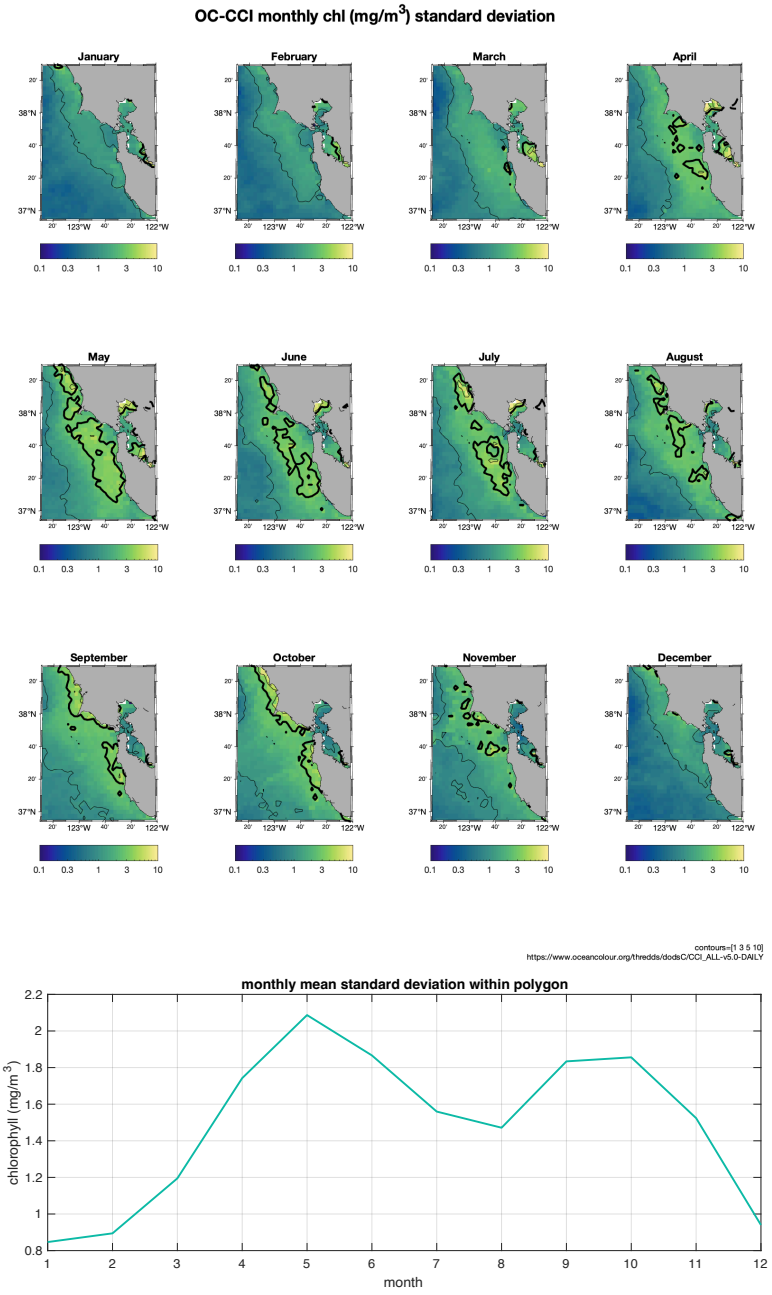

Figure 8. Chlorophyll (mg/m^3) monthly standard deviation (above) and time series of the monthly mean standard deviation (below). Monthly means were calculated using the OC-CCI daily chlorophyll product (1997-2021). Contours represent where chlorophyll concentrations are 1, 3, 5, and 10 mg/m^3. The thicker contour line is at 3 mg/m^3. Labeled color bars are beneath each subplot.

has been described here, as shown by the large 95% confidence interval compared to the mean in Figure 7. January, February, and August are the only months with which anomalously low mean chlorophyll concentrations remain above zero within the 95% confidence interval. In May, the mean can get as high as 7.41 mg/m^3, and similarly in September, the mean can reach values as high as 7.23 mg/m^3. From December–February the range is not as wide, with the least variable month being January. At that time, the mean can reach anomalous lows around 0.16 mg/m^3 and anomalous highs around 3.55 mg/m^3.

Compared with the monthly means, standard deviations show a similar trend, with the smallest values occurring during the winter and ranging from 0.85-0.94 mg/m^3, and the largest standard deviation appearing in springtime—particularly in May—when the mean standard deviation within the Gulf is 2.09 mg/m^3. The month with the second highest mean standard deviation is October, with a value of 1.86 mg/m^3. In September and October, maximum standard deviation is almost exclusively present along the coast, whereas from May–July, its largest offshore.

4.1.4 EOFs

At an 80% threshold, 834 out of 1,120 frames—or ~74.5%—were kept and used to calculate the chlorophyll EOFs (Figures 9 & 10). From those 834 frames, the time series spans from September 30, 1997 to December 27, 2021.

Mode 1 of the linear EOF (Fig. 9) accounted for ~36.5% of the variability in chlorophyll within our study area, mode 2 for ~13.8%, mode 3 for ~7.0%, and mode 4 accounted for ~4.5%. Together, the first four modes explained approximately 61.9% of the variability in the data. For the log-transformed EOF (Fig. 10), mode 1 accounted for ~40.2% of the variability in chlorophyll within our study area, mode 2 for ~16.2%, mode 3 for ~7.6%, and mode 4 accounted for ~ 3.7%. Cumulatively, the first four modes explained approximately 67.7% of the variability in the data. The first four modes of the linear and

log-transformed EOFs individually show similar qualitative patterns in chlorophyll, and explain similar proportions of the total variability. We focused on these four modes because of their similarities. Higher modes were more variable between linear and log-transformed data, and of course also accounted for smaller fractions of variability.

Mode 1 is a single-signed pattern in which chlorophyll increases or decreases throughout the study region with largest amplitude in the center and lowest amplitude at the mouth of San Francisco Bay and outer slope waters. Mode 2 shows a north-south split indicating that chlorophyll changes in opposite directions to the north or south of the Golden Gate (37.8°N). Mode 3 presents an onshore-offshore structure in which chlorophyll increases or decreases oppositely as one moves cross-shore. Mode 4 offers a three-way split in which chlorophyll varies oppositely in the Gulf of the Farallones than north of Pt. Reyes and offshore of Half Moon Bay (37.5°N), and in the log-transformed EOF, seaward of the Farallon Islands (37.7°N).

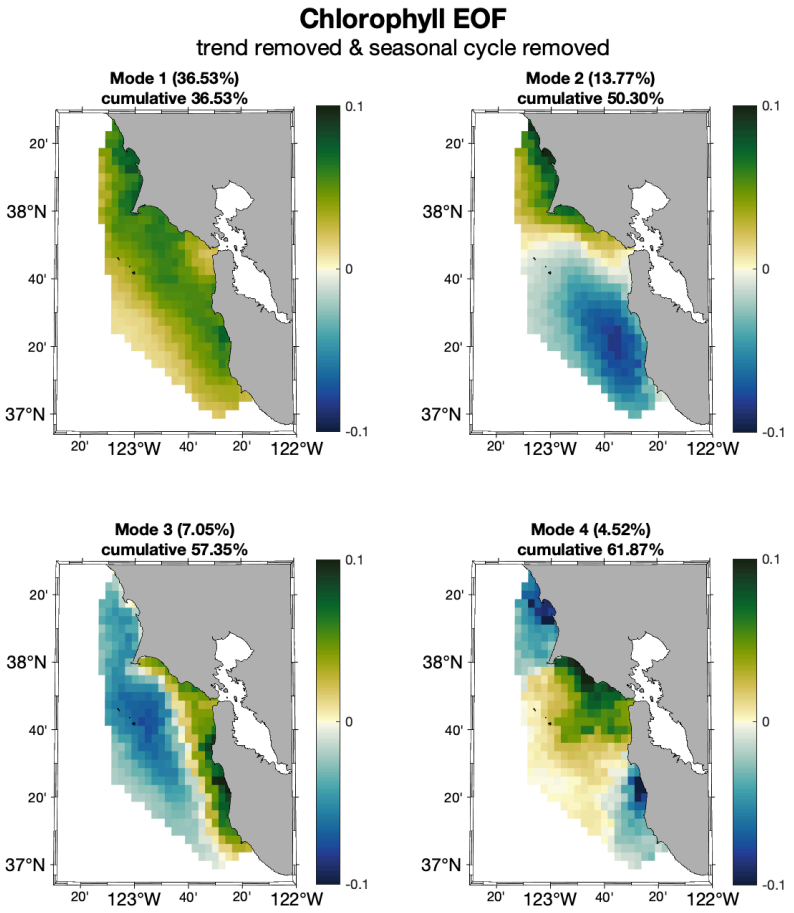

Figure 9. First 4 modes of the linear chlorophyll EOF. The eigenvectors at each pixel are plotted for each mode. In the title of each subplot is the mode and percent of variability and cumulative variability explained by that mode. A labeled color bar is to the right of each subplot. The trend and seasonal cycle were removed prior to calculating the EOF.

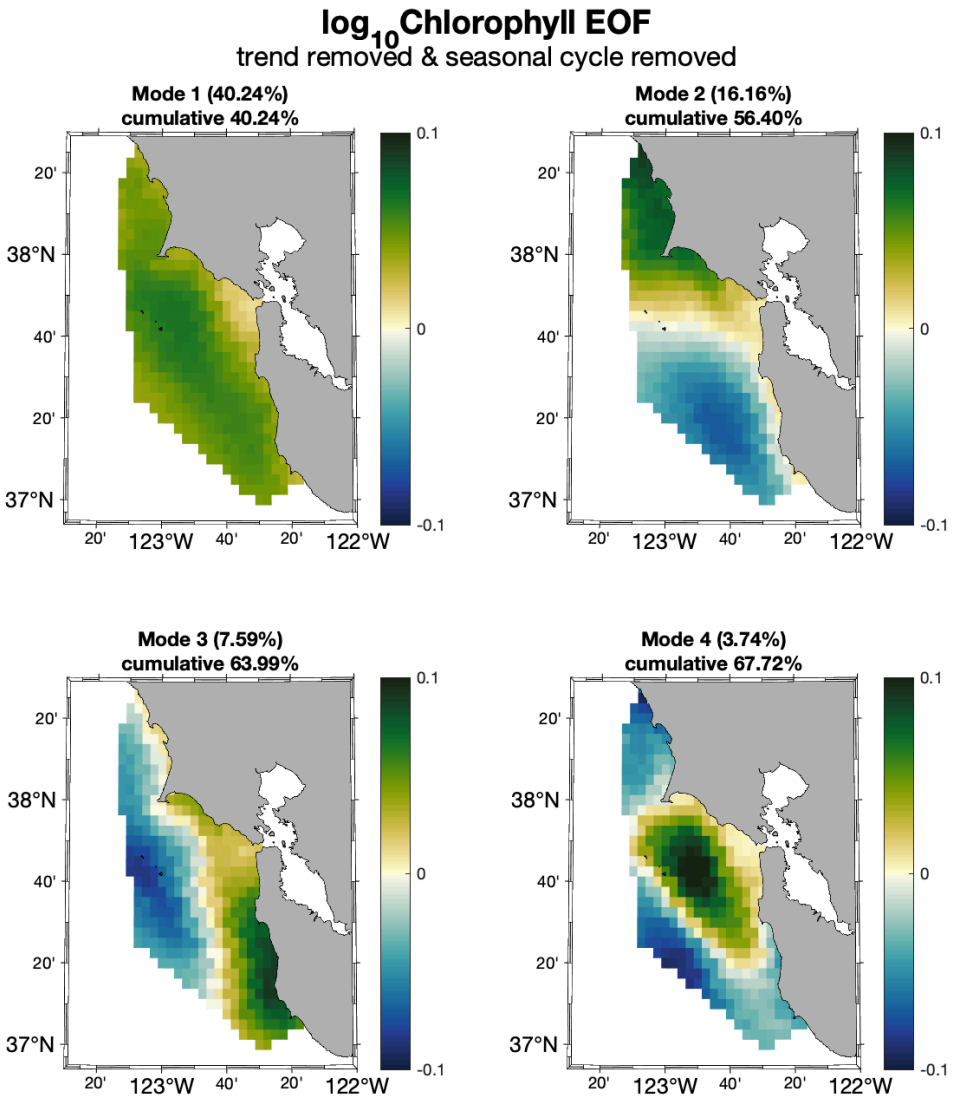

Figure 10. First 4 modes of the log-transformed chlorophyll EOF. The eigenvectors at each pixel are plotted for each mode. In the title of each subplot is the mode and percent of variability and cumulative variability explained by that mode. A labeled color bar is to the right of each subplot. The trend and seasonal cycle were removed prior to calculating the EOF.

4.1.5 Amplitude time series

Seasonal cycles of the modal amplitudes for the first four modes in the linear and log-transformed chlorophyll EOFs are shown as times series in Figures 11 and 12, respectively. Although the amplitude of each mode does vary during some months—particularly for modes 1, 3, and 4 of the log-transformed chlorophyll—sometimes showing a positive tendency and sometimes showing a negative tendency, there is considerable variability in the modal amplitude within each month as indicated by the large standard error around the mean in each case. None of the modes in either EOF show a clear distinctly non-zero amplitude on a monthly basis. Though it is not as evident in the linear data, mode 4 for the log-transformed data has a positive value in April about 87% of the time. This tendency indicates that during that month, chlorophyll concentrations in the Gulf of the Farallones are relatively high compared to regions north of Pt. Reyes, south of Half Moon Bay, and beyond the shelf break. The fact that the standard error of all modes extend across zero suggests considerable variability of all of these modes throughout each month.

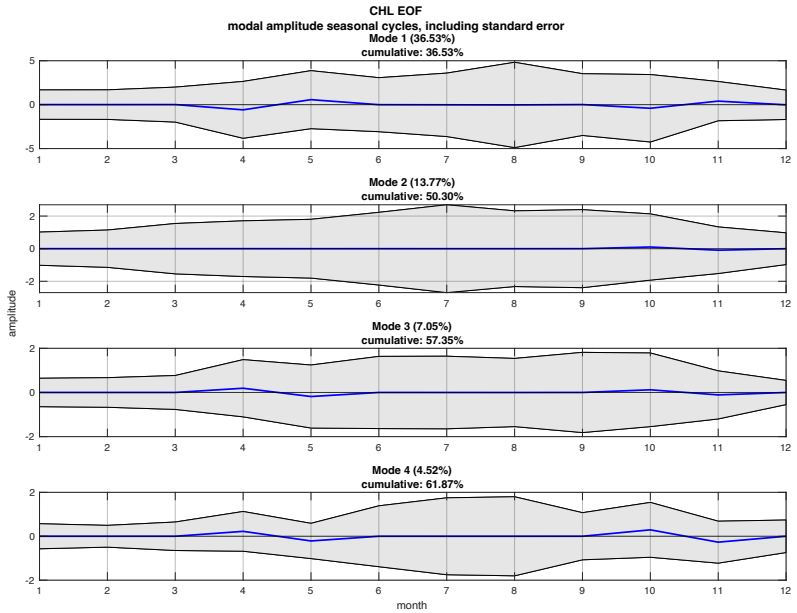

Figure 11. Monthly mean amplitudes for modes 1-4 of the linear chlorophyll EOF. The grey shaded region represents the standard error. The mode, and percent of variability and cumulative variability explained by that mode, are in the title of each time series.

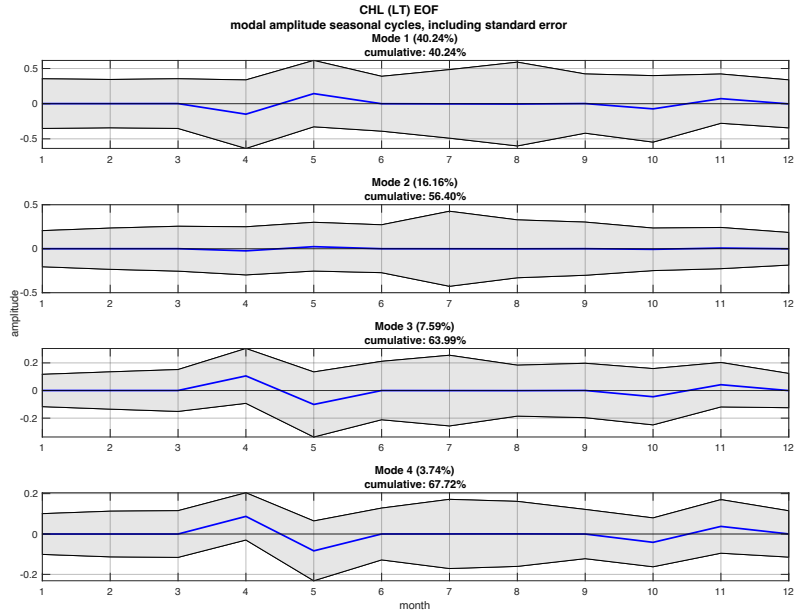

Figure 12. Monthly mean amplitudes for modes 1-4 of the log-transformed chlorophyll EOF. The grey shaded region represents the standard error. The mode, and percent of variability and cumulative variability explained by that mode, are in the title of each subplot.

4.1.6 Multivariate anecdotal descriptions

Frames were chosen anecdotally to display differing patterns in chlorophyll within the study region, as well as surface currents and sea surface temperature on those same dates (Fig. 13). On April 15, 2017, a strong chlorophyll signal was present throughout most of our area of interest. Surface currents on that same day generally flowed in the offshore direction, and sea surface temperature was largely uniform within the same region. On June 1, 2012, the chlorophyll signal outside of SF Bay extended primarily to the south. Surface currents on this day also generally moved water equatorward, and a plume of relatively warm water appeared to exit from SF Bay. The opposite scenario occurred on January 17, 2017. The chlorophyll signal on this day extended to the north past our study domain, surface currents were likewise pointing poleward, and a plume of relatively cool water appearing to have exited SF Bay filled the northern half of our study region. On November 17, 2013, the chlorophyll plume was only present from just north of Pt. Reyes to just south of Half Moon Bay, and reached just past the Farallon Islands at its offshore boundary. Surface currents on this day primarily moved waters offshore; however, although not obvious, a cyclonic shelf circulation structure was present at and south of the Pt. Reyes headland. North of Pt. Reyes, surface currents pointed poleward. Sea surface temperatures were warmest south of Half Moon Bay and offshore, and coolest near Bodega Bay (38.3°N) north of Pt. Reyes. Within the region of the cyclonic circulation structure are some patches of warmer water. The temperature within the Gulf of the Farallones on this day appears to be unrelated to SF Bay outflow.

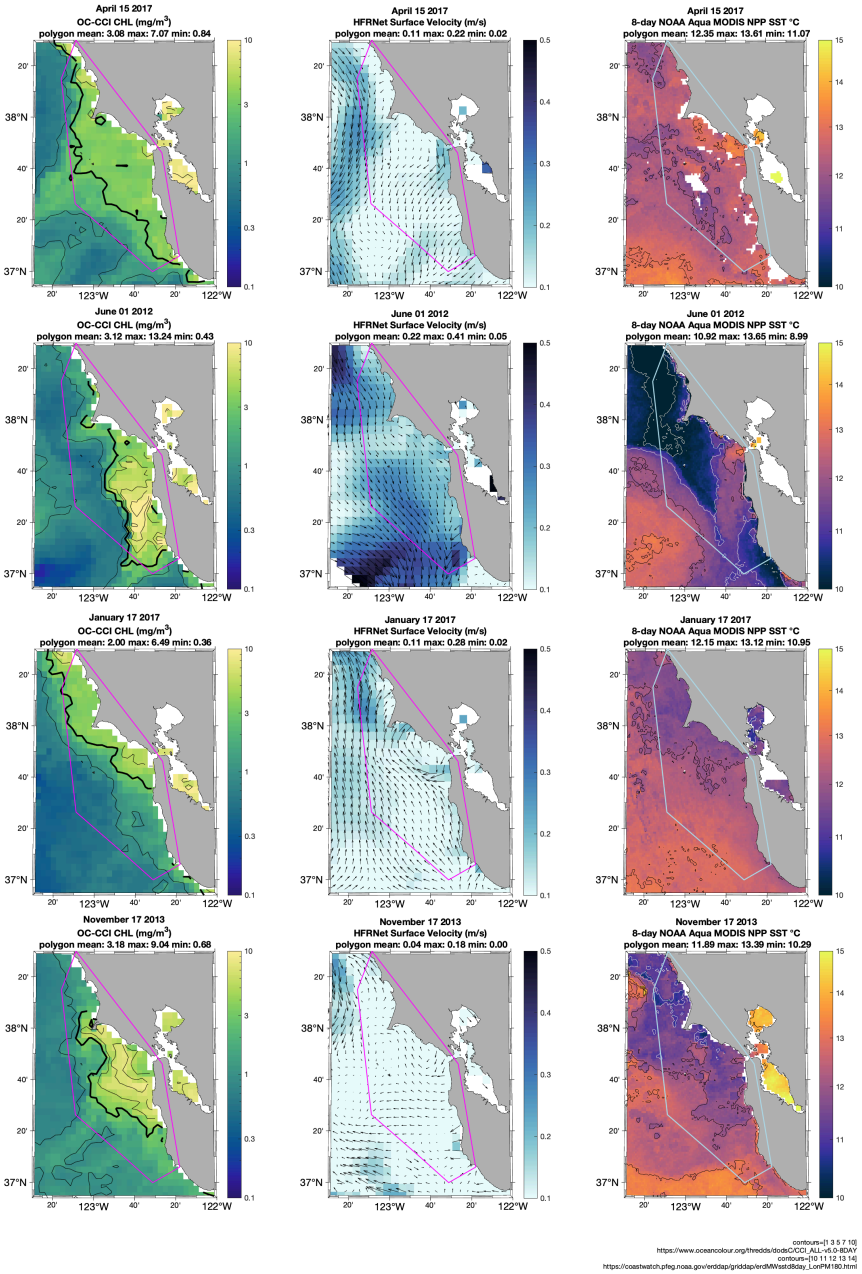

Figure 13. Snapshots of 8-day chlorophyll (mg/m^3), 8-day HFR (m/s), and 8-day SST (°C) composites on dates which display differing patterns in chlorophyll within the area of interest (outlined in pink for chl and HFR, and light blue for SST). Labeled color bars are to the right of each subplot. The date, product, mean, maximum, and minimum within the polygon are written in the title of each subplot. Contours for chlorophyll are at 1, 3, 5, 7, and 10 mg/m^3. The thicker contour is at 3 mg/m^3. Contours for SST are at 10, 11, 12, 13, and 14°C. The white contours are at 10 and 11°C.

4.2 Surface currents

4.2.1 Monthly climatology

The monthly climatology of surface velocities within the study domain is shown in Figure 14. During late fall and early to mid-winter (November–January), mean surface currents are relatively slow and flow primarily offshore. They begin to flow more equatorward and pick up speed in February, reaching their highest velocities from April–June, particularly north of Pt. Reyes. That said, surface currents in the overall area of interest travel fastest in April, flowing almost exclusively equatorward that month. Circulation in the offshore southern region of the domain begins to turn more offshore in May. This offshore flow also occurs inshore in June, and more northward with each coming month. Waters immediately exiting SF Bay appear to travel primarily equatorward from February–October, with some additional poleward flow from November–January within the Gulf of the Farallones, particularly in December.

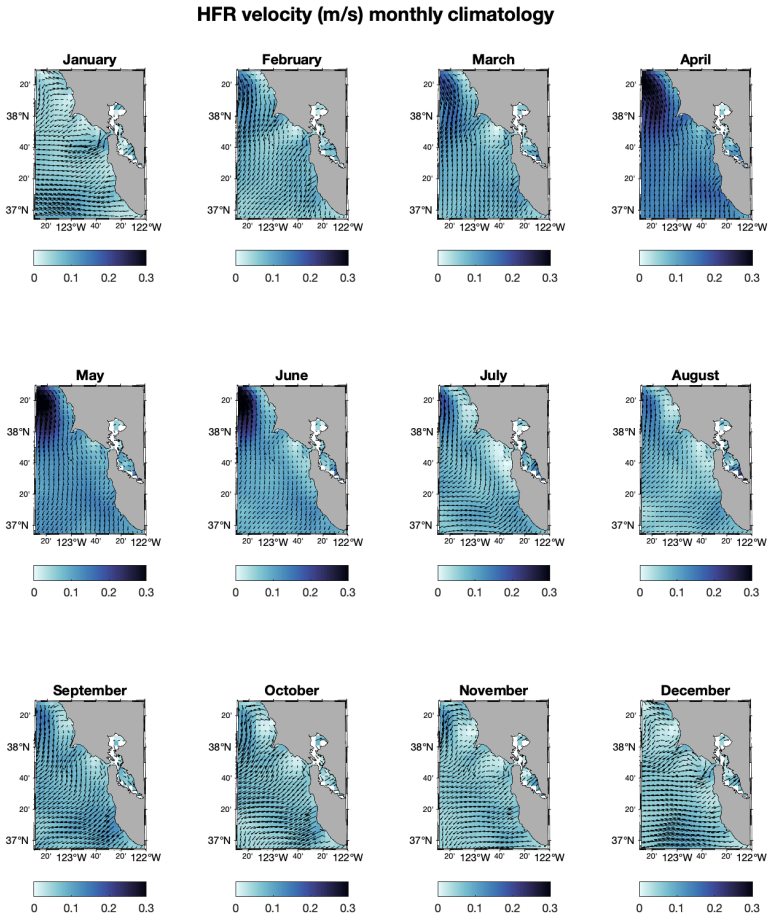

Figure 14. HFR surface current (m/s) monthly climatology. Monthly means were calculated using 25-hour averages of the hourly HFRNet product (2012-2022). Labeled color bars are beneath each subplot.

4.2.2 EOF

At a 99% threshold, 3,269 out of 3,720 frames—or ~88%—were kept and used to calculate the HFR EOF (Fig. 15). From those 3,269 frames, the time series spans from January 6, 2012 to June 2, 2022.

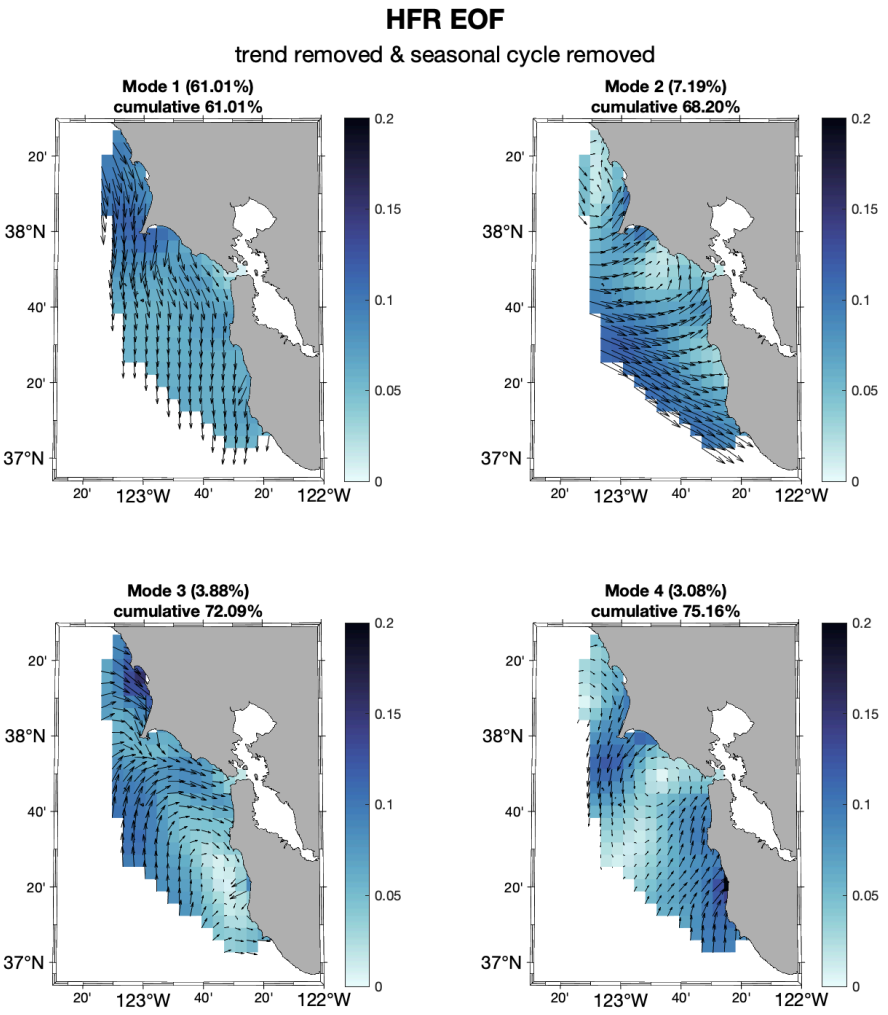

Figure 15. First 4 modes of the HFR EOF. The eigenvectors at each pixel are plotted for each mode. In the title of each subplot is the mode and percent of variability and cumulative variability explained by that mode. Arrows indicate the direction of flow, and the length of the arrows indicate the strength of flow relative to that subplot. Color is indicative of speed. This analysis was performed on 25-hour averaged data and the trend and seasonal cycle were removed prior to calculating the EOF.

Mode 1 accounted for ~61.0% of the variability in surface velocities within our study area, mode 2 accounted for ~7.2%, mode 3 accounted for ~3.9%, and mode 4 accounted for ~3.1%. Together, the first four modes explained approximately 75.2% of the variability in the data.

An approximately uniform alongshore flow in which surface currents travel alongshore, either poleward or equatorward, throughout the study region is present in

mode 1. Mode 2 presents a more complex structure. Beginning near the shelf break toward the center edge of the domain, there is an offshore band of relatively strong alongshore flow traveling south and veering toward the coast. Near Mavericks (37.5°N) that flow begins to turn onshore toward the SF Bay inlet, where the onshore flow turns poleward. Here, offshore currents travel onshore where they meet that inshore poleward flow. North of Pt. Reyes, inshore flow is also poleward, while offshore flow just inside the study region travels equatorward. All of these features vary oppositely to one another. Mode 3 features a relatively large circulation structure that is either anticyclonic (shown) or cyclonic, centered offshore Half Moon Bay. The circulation pattern encompasses the waters to the north of its center, until just south of the Pt. Reyes headland. North of Pt. Reyes, surface currents closest to the shoreline are traveling equatorward (shown) or poleward, while those offshore are traveling onshore (shown) or offshore. South of Pigeon Point (37.1°N), flow breaks off from the anticyclonic/cyclonic circulation structure and begins to turn equatorward/poleward. Mode 4 displays a more well-defined circulation structure that is again either anticyclonic or cyclonic (shown). The center of this eddy-like structure is located in the Gulf of the Farallones. It appears that there may be another eddy-like structure centered offshore Bodega Bay at the shelf break that circulates oppositely to the one located in the Gulf. Flow from that structure appears to join the structure within the Gulf at the cape of Pt. Reyes.

The mean monthly modal amplitude for all four modes is close to zero relative to the calculated standard error, which indicates large variability over short time scales within each month. Even for those months that do show a slight positive or negative mean amplitude, the standard error of all modes extends considerably across zero.

4.3 Sea surface temperature

4.3.1 Monthly climatology

The monthly climatology of sea surface temperature within the study domain is shown in Figure 16. Sea surface temperatures within SF Bay are coolest in the winter months (December–February), reaching their coolest temperatures in January, the only month with which SF Bay waters are on average cooler than the surrounding coastal ocean in the Gulf of the Farallones. December and February, on the other hand, are the only months in which SST in the Bay and the Gulf are comparable. Bay waters are warmest from late spring to early fall (June–September), reaching their maximum temperatures in June. As this relatively warm water exits the

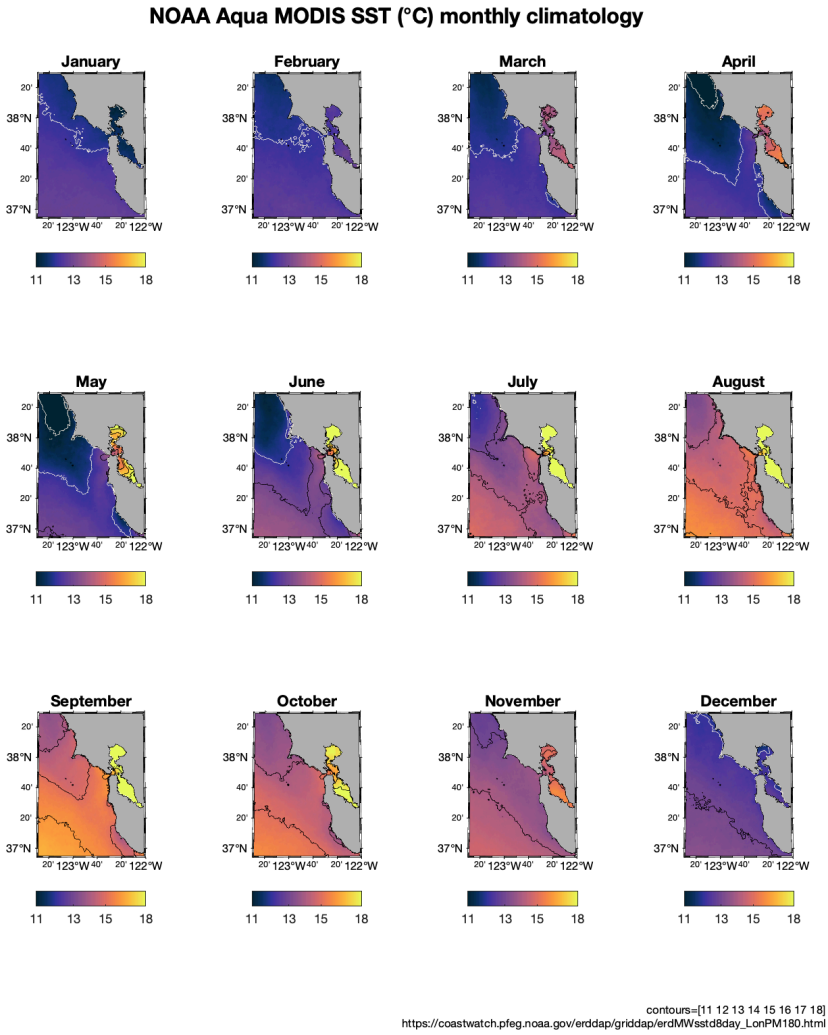

Figure 16. Sea surface temperature (°C) monthly climatology. Monthly means were calculated using the 8-day NOAA MODIS Aqua product (2002-2022). Contours represent where SSTs are 10, 11, 12, 13, 14, 15, 16, 17, and 18°C. Labeled color bars are beneath each subplot.

Golden Gate during springtime and enters into the surrounding coastal ocean, a tongue of cool water simultaneously enters the Gulf of the Farallones from the north, making April and May the Gulf's coolest months on average with respect to sea surface temperature, reaching lows of 11.72°C and 11.81°C, respectively. Waters within the Gulf begin to warm from summer to early fall, reaching their highest mean temperatures of 14.98°C in the month of September. In general, SF Bay warms to relatively high temperatures sooner in the year than in the Gulf, and although the Gulf does fluctuate in temperature throughout the year, it never reaches the maximum temperatures observed within SF Bay.

4.3.2 EOF

Using an 80% threshold, 4,801 out of 6,560 frames—or ~73%—were kept and used to calculate the SST EOF (Fig. 17). From those 4,801 frames, the time series spans from July 5, 2002 to March 25, 2022.

Mode 1 accounted for ~76.9% of the variability in sea surface temperature within our study area, mode 2 accounted for ~3.5%, mode 3 accounted for ~2.5%, and mode 4 accounted for ~1.4%. Together, the first four modes explained approximately 84.2% of the variability in the data.

The first mode is an almost entirely uniform single-signed pattern in which SST either increases or decreases throughout the study region. Mode 2 shows a north-south split indicating that SST changes in opposite directions to the north or south of the Golden Gate. Mode 3 presents an onshore-offshore structure in which SST increases or decreases oppositely as one moves cross-shore, particularly south of Pt. Reyes. Mode 4 illustrates a three-way split in which SST varies oppositely in the Gulf of the Farallones and seaward of the Farallon Islands than offshore Half Moon Bay and in waters from just south of Pt. Reyes along the coast in Drakes Bay (38°N) to the northernmost area of our study region. The largest positive amplitudes, however, are in the region offshore Half Moon Bay.

Similar to the previous EOFs, the mean monthly modal amplitude for all four SST modes is close to zero relative to the calculated standard error, which again indicates large variability over short time scales within each month.

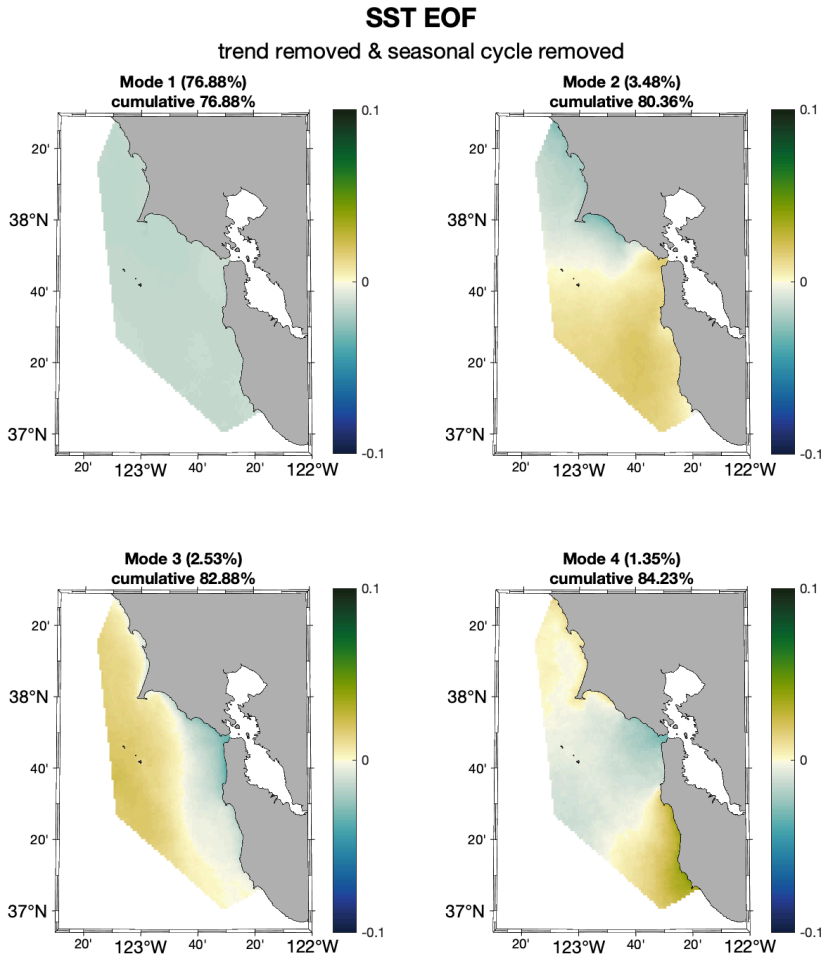

Figure 17. First 4 modes of the SST EOF. The eigenvectors at each pixel are plotted for each mode. In the title of each subplot is the mode and percent of variability and cumulative variability explained by that mode. A labeled color bar is to the right of each subplot. The trend and seasonal cycle were both removed prior to calculating the EOF.

4.4 EOF correlations

4.4.1 Chlorophyll & HFR

4.4.1.1 EOFs

Using an 85% threshold for chlorophyll and a 99% threshold for surface currents, 310 out of 397 frames—or ~78%—were retained to calculate new univariate EOFs for chlorophyll and HFR (Fig. 18). We restate that these EOFs were univariate as shown previously, but using only these 310 frames when both time-series had data simultaneously. This new time series spans from February 26, 2012 to December 27, 2021.

For the chlorophyll EOF, mode 1 explained ~40.2% of the variability in $\log_{10}$(chlorophyll) within our study area, mode 2 accounted for ~17.3%, mode 3 accounted for ~6.1%, and mode 4 accounted for ~4.0%. Together, the first four modes explained approximately 67.6% of the variability in the data.

For the HFR EOF, mode 1 explained ~52.9% of the variability in surface velocities within our study area, mode 2 accounted for ~7.0%, mode 3 accounted for ~6.2%, and mode 4 accounted for ~4.4%. Together, the first four modes explained approximately 70.6% of the variability in the data.

Figure 18. First 4 modes of the log-transformed chlorophyll EOF (upper) and first 4 modes of the HFR EOF (lower) used for correlation analysis. The eigenvectors at each pixel are plotted for each mode. Arrows indicate the direction of flow, and the length of the arrows indicate the strength of flow relative to the rest of the flow in that subplot. For the HFR EOF, color is indicative of speed. In the title of each subplot is the mode and percent of variability and cumulative variability explained by that mode. A labeled color bar is to the right of each subplot. The trend and seasonal cycle were removed prior to calculating each EOF.

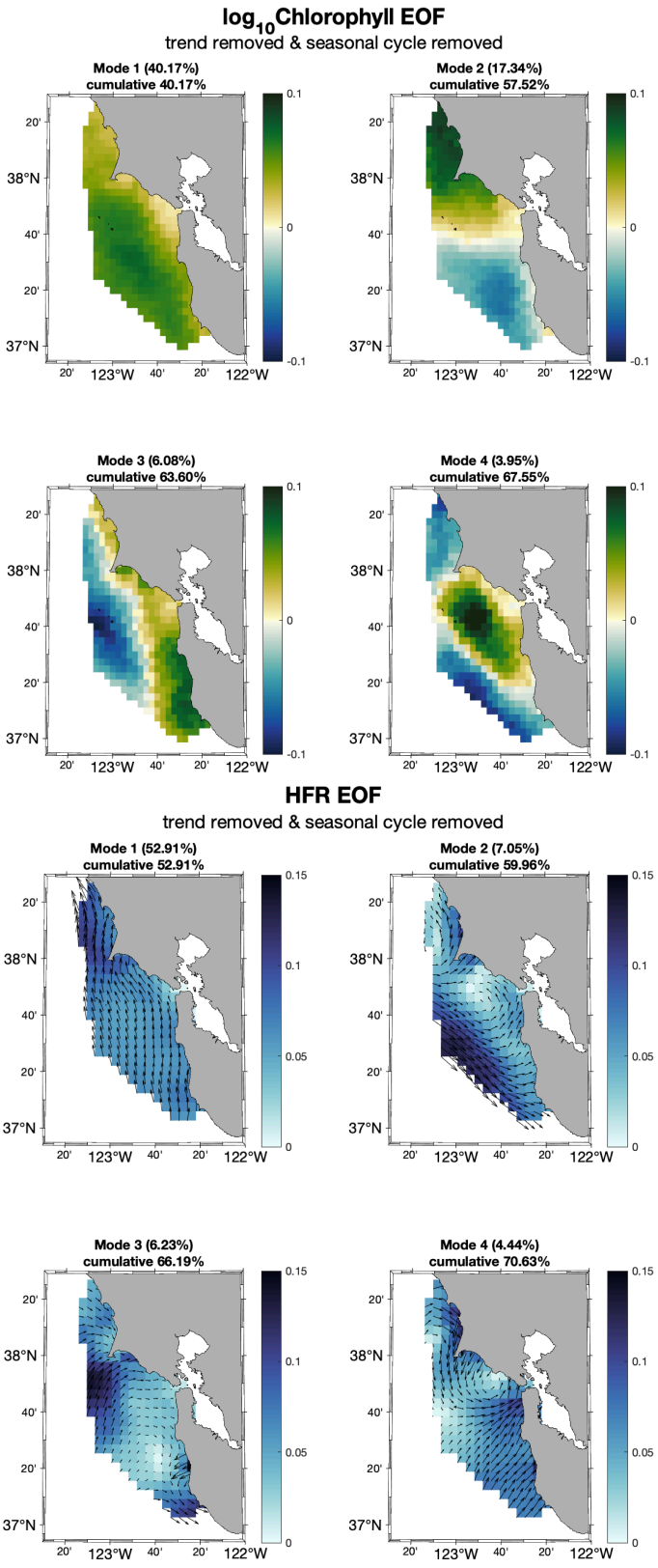
log10Chlorophyll EOF
trend removed & seasonal cycle removed
Mode 1 (40.17%)
cumulative 40.17%
Mode 2 (17.34%)
cumulative 57.52%
Mode 3 (6.08%)
cumulative 63.60%
Mode 4 (3.95%)
cumulative 67.55%
HFR EOF
trend removed & seasonal cycle removed
Mode 1 (52.91%)
cumulative 52.91%
Mode 2 (7.05%)
cumulative 59.96%
Mode 3 (6.23%)
cumulative 66.19%
Mode 4 (4.44%)
cumulative 70.63%
38°N
37°N
123°W
122°W
20'
40'

The patterns illustrated by the first four modes of the log-transformed chlorophyll EOF in this case closely resemble that of the previous chlorophyll EOFs—both linear and log-transformed—shown in Figures 9 and 10. To reiterate, mode 1 is approximately a single-signed pattern in which chlorophyll increases or decreases throughout the study region. Largest amplitude in this case is offshore and lowest amplitude is near the coast, particularly from the mouth of San Francisco Bay to north of Pt. Reyes. Mode 2 is again a north-south split indicating a change in chlorophyll that varies oppositely to the north and south of the Golden Gate. Mode 3 shows an onshore-offshore structure in which chlorophyll increases or decreases oppositely as one moves cross-shore. Mode 4 presents a three-way split in which chlorophyll varies oppositely in the Gulf of the Farallones than north of Pt. Reyes, offshore of Half Moon Bay, and seaward of the Farallon Islands.

Likewise, the HFR EOF in this case is also similar to the previous EOF of surface currents shown in Figure 15, despite the fact that this one was produced by an 8-day composite while the one shown previously was produced by a larger number of 25-hour averages. Mode 1 again shows an approximately uniform alongshore flow in which surface currents travel either poleward or equatorward throughout the study region. Modes 2-4, however, present more complex structures. In Mode 2, beginning near the shelf break toward the center edge of the domain is a band of relatively strong alongshore flow that travels south/north and veers toward/away from the coast. Near Mavericks, that alongshore flow begins to turn cross-shore either toward or away from the SF Bay inlet, where it then turns either poleward or equatorward. At the same latitude, currents offshore travel cross-shore where they meet the inshore poleward/equatorward flow. It appears that there may be an eddy-like circulation feature centered in the middle of the Gulf of the Farallones. North of Pt. Reyes, inshore flow is also poleward/equatorward, while offshore flow just inside the study domain travels in the opposite direction.

Mode 3 features a relatively large circulation structure centered offshore Half Moon Bay and encompassing the waters to the north of its center. Surface currents exit this shelf circulation structure near the Gulf of the Farallones and begin to travel onshore toward the mouth of SF Bay (shown) or offshore, exiting the mouth of SF Bay. Farther south, there appears to be some strong cross-shore flow along the coast near San Gregorio (37.3°N). South of Pigeon Pt., flow breaks off from/joins the anticyclonic/cyclonic circulation structure and begins to travel equatorward/poleward. Mode 4 also displays a circulation structure that is again either anticyclonic or cyclonic (shown). The center of this structure is located directly next to the coast near Duxbury Point (37.9°N) in the Gulf of the Farallones. North of Pt. Reyes, it appears that there may be another eddy-like structure centered offshore near the shelf break between Bodega Bay and Pt. Reyes that circulates oppositely to the one located in the Gulf. Flow from that structure appears to join the structure within the Gulf near the Pt. Reyes headland. In the southern half of the domain, surface currents flow approximately cross-shore either toward or away from the Golden Gate.

4.4.1.2 Amplitude time series

Seasonal cycles of the modal amplitudes for the first four modes in the log-transformed chlorophyll and HFR EOFs calculated for correlation analysis are shown as times series in Figure 19. Although none of the modes in either EOF show a clear distinctly non-zero amplitude on a monthly basis, there are some notable features worth mentioning.

Mode 1 of the chlorophyll EOF is negative in April about 81% of the time and positive in May about 85% of the time, suggesting that it is common in the month of April for chlorophyll to be uniformly absent or have relatively low concentrations throughout our domain, while the opposite is true for May, when relatively high concentrations are expected. Mode 3 is positive in April about 87% of the time and

negative in November about 80% of the time. This tendency suggests that it is typical in April for the chlorophyll signal to be exclusively present more onshore over the shelf, while in November relatively high chlorophyll concentrations are typically located exclusively more offshore. Similar to what was illustrated in Figure 12, Mode 4 is positive in April about 92% of the time, again indicating that during that month, chlorophyll concentrations in the Gulf of the Farallones are relatively high in comparison to regions north of Pt. Reyes, south of Half Moon Bay, and beyond the shelf break.

Mode 3 of the HF Radar EOF is negative in May 97% of the time. This finding suggests that the circulation structure centered offshore Half Moon Bay is almost always cyclonic in the month of May. Additionally, near the Gulf of the Farallones, water is typically exiting the SF Bay inlet during this month. Surface velocities are moving onshore along the coast near San Gregorio, and south of Pigeon Pt., flow travels poleward where it eventually joins the cyclonic shelf circulation structure. All that said, the fact that the standard error of all modes in both EOFs extend across zero again suggests considerable variability of all of these modes throughout each month.

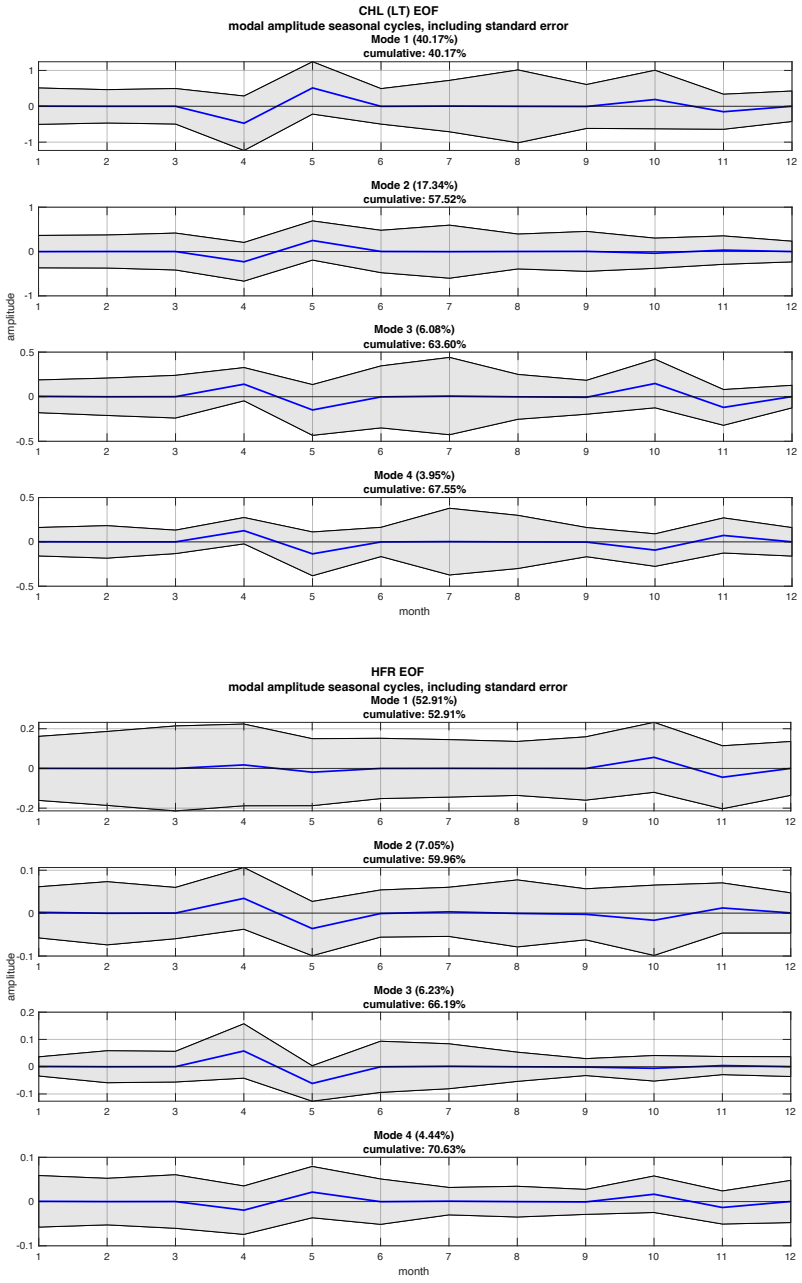

Figure 19. Monthly mean amplitudes for modes 1-4 of the log-transformed chlorophyll EOF and HFR EOF calculated for correlation analysis. The grey shaded region represents the standard error. The mode, and percent of variability and cumulative variability explained by that mode, are in the title of each time series.

4.4.2 Chlorophyll & SST

4.4.2.1 EOFs

At an 80% threshold for chlorophyll and a 75% threshold for sea surface temperature, 557 out of 794 frames—or ~70%—were kept and used to calculate new univariate EOFs for chlorophyll and SST, this time with matching time series (Fig. 20). From those 557 frames, the time series spans from July 20, 2002 to December 27, 2021.

For the chlorophyll EOF, mode 1 explained ~37.6% of the variability in $\log_{10}$(chlorophyll) within our study area, mode 2 accounted for ~16.7%, mode 3 accounted for ~7.8%, and mode 4 accounted for ~4.0%. Together, the first four modes explained approximately 66.1% of the variability in the data.

For the SST EOF, mode 1 explained ~78.3% of the variability in sea surface temperature within our study area, mode 2 accounted for ~3.4%, mode 3 accounted for ~2.5%, and mode 4 accounted for ~1.2%. Together, the first four modes explained approximately 85.4% of the variability in the data.

Figure 20. First 4 modes of the log-transformed chlorophyll EOF (upper) and first 4 modes of the SST EOF (lower) used for correlation analysis. The eigenvectors at each pixel are plotted for each mode. In the title of each subplot is the mode and percent of variability and cumulative variability explained by that mode. A labeled color bar is to the right of each subplot. The trend and seasonal cycle were removed prior to calculating each EOF.

$\log_{10}$Chlorophyll EOF

trend removed & seasonal cycle removed

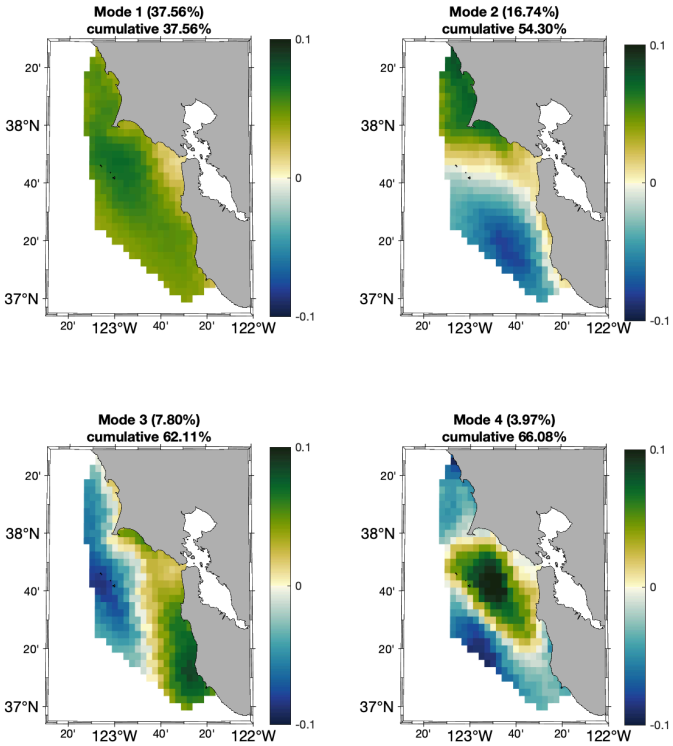

SST EOF

trend removed & seasonal cycle removed

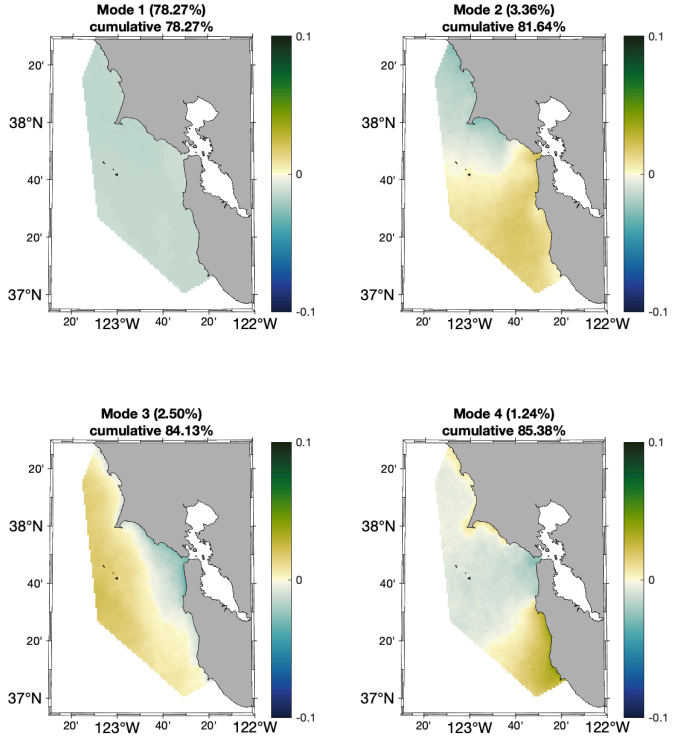

Here, the first four modes of the log-transformed chlorophyll EOF display again the same patterns previously illustrated and described (Figs. 9, 10, and 18). Similarly, the SST EOF in this case closely resembles the modes shown in Figure 17. Mode 1 is again single-signed and almost entirely uniform, describing a pattern in which SST either increases or decreases throughout the study region. Mode 2 shows a north-south split indicating that SST changes in opposite directions to the north or south of the Golden Gate. Mode 3 presents an onshore-offshore structure in which SST increases or decreases oppositely as one moves cross-shore, particularly south of Pt. Reyes and north of Pescadero (37.3°N). Of all four modes, mode 4 in Figure 20 presents the largest difference in spatial pattern than what is shown in Figure 17. SST varies oppositely south of Pt. San Pedro and along the shoreline north of Duxbury Pt. than in the Gulf of the Farallones, seaward of the Farallon Islands beyond the shelf break, and offshore Bodega Bay.

4.4.2.2 Amplitude time series

Seasonal cycles of the modal amplitudes for the first four modes in the log-transformed chlorophyll and SST EOFs are shown as times series in Figure 21. Mode 3 of the chlorophyll EOF is positive in April about 82% of the time and negative in May about 82% of the time, suggesting that high concentrations of chlorophyll are commonly present exclusively onshore in April and offshore in May. Mode 4 is positive in April about 81% of time, once again indicating that during that month, chlorophyll concentrations in the Gulf of the Farallones are relatively high in comparison to regions north of Pt. Reyes, south of Half Moon Bay, and beyond the shelf break.

For the SST EOF, mode 1 is positive in June about 96% of the time, negative in September about 89% of the time, and negative in November about 90% of the time. This tendency suggests that sea surface temperatures are almost always uniformly relatively cool throughout our domain in June, while relatively warm in September and

November. Mode 3 is always positive in both January and December, indicating that SST is always relatively cool onshore and relatively warm offshore during those months. In March, mode 3 is negative about 94% of the time. This propensity implies that SST is typically relatively warm onshore and relatively cool offshore in March. Mode 4 is positive in January about 99% of the time, suggesting that during that month, SST is almost always relatively warm south of Pt. San Pedro and along the shoreline north of Duxbury Pt., while relatively cool in the Gulf of the Farallones, seaward of the Farallon Islands beyond the shelf break, and offshore Bodega Bay. Conversely, in November, mode 4 is negative about 84% of the time, suggesting that it is typical for the opposite to be true in November than in January.

Across both EOFs, the only mode that shows a distinctly non-zero amplitude on a monthly basis is SST mode 3, specifically in January and December. In every other case, the large standard error that extends across zero suggests considerable variability of all of these modes throughout each of those months.

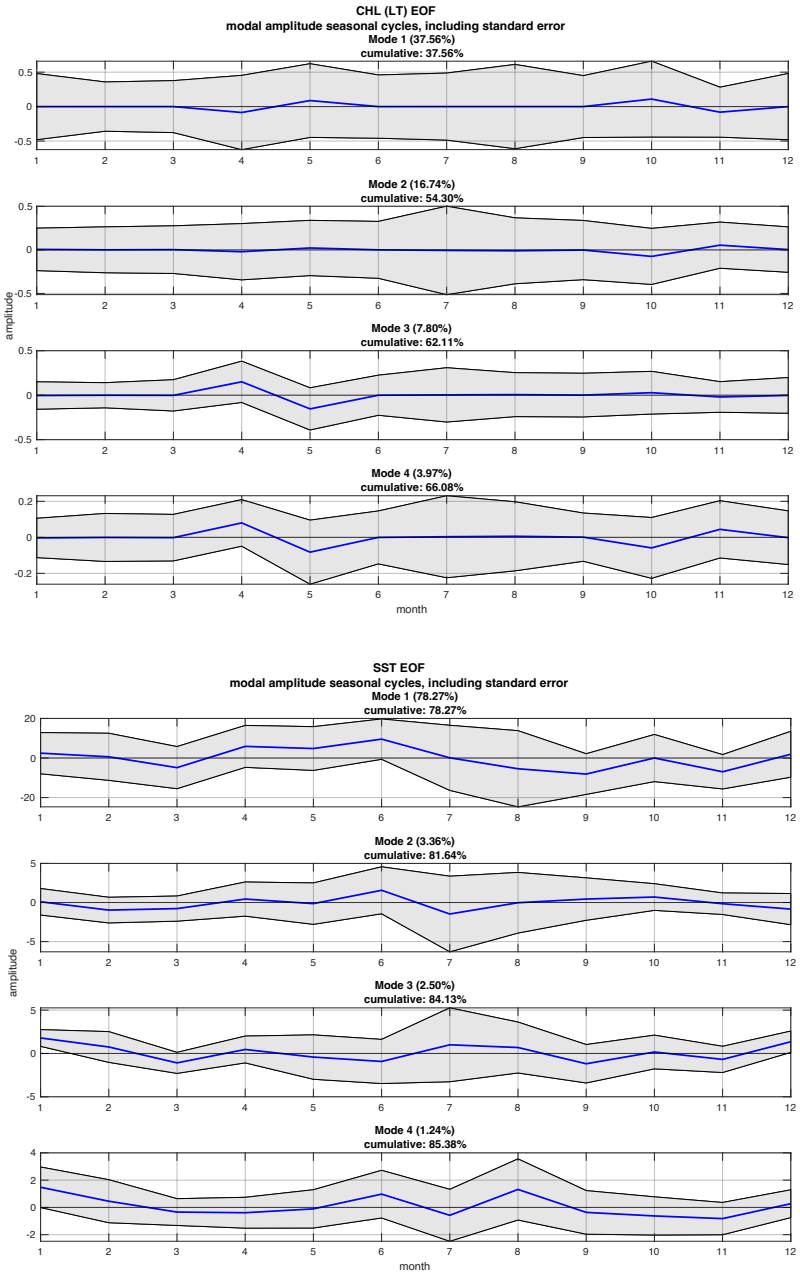

Figure 21. Monthly mean amplitudes for modes 1-4 of the log-transformed chlorophyll EOF and SST EOF calculated for correlation analysis. The grey shaded region represents the standard error. The mode, and percent of variability and cumulative variability explained by that mode, are in the title of each time series.

4.4.3 Correlations

For chlorophyll and HFR, the correlation coefficient was statistically significant at the 5% level for chl mode 1 and HFR modes 1 (H_0: r = 0; r = -0.13; p = 0.02) and 4 (H_0: r = 0; r = -0.19; p = 0.00), chl mode 2 and HFR modes 1 (H_0: r = 0; r = 0.48; p = 0.00), 2 (H_0: r = 0; r = -0.14; p = 0.01), and 3 (H_0: r = 0; r = -0.13; p = 0.03), chl mode 3 and HFR mode 2 (H_0: r = 0; r = 0.21; p = 0.00), and chl mode 4 and HFR mode 2 (H_0: r = 0; r = 0.13; p = 0.03). Therefore, for each of these, the null hypothesis that no relationship exists between patterns in chlorophyll and surface currents was rejected. We failed to reject the null hypothesis for the remaining unhighlighted correlations shown in Table 1.

For chlorophyll and SST, the correlation coefficient was statistically significant at the 5% level for chl mode 1 and SST mode 1 (H_0: r = 0; r = 0.09; p = 0.05), chl mode 2 and SST modes 1 (H_0: r = 0; r = -0.35; p = 0.00), 2 (H_0: r = 0; r = -0.25; p = 0.00), 3 (H_0: r = 0; r = 0.18; p = 0.00), and 4 (H_0: r = 0; r = 0.16; p = 0.00), chl mode 3 and SST mode 1 (H_0: r = 0; r = 0.19; p = 0.00), and chl mode 4 and SST modes 1 (H_0: r = 0; r = 0.17; p = 0.00) and 4 (H_0: r = 0; r = 0.10; p = 0.02). Therefore, for each of these, the null hypothesis that no relationship exists between patterns in chlorophyll and sea surface temperature was rejected. We failed to reject the null hypothesis for the remaining correlations shown in Table 1.

Table 1. Pearson's r values and their associated p-values from EOF correlation analysis. All chlorophyll was log-transformed. Results with p-values < 0.05 are bolded. Correlations with r values ≥ |0.1| are highlighted in pink and correlations with r values ≥ |0.3| are highlighted in purple.

	chl mode 1		chl mode 2		chl mode 3		chl mode 4	
	r	p-value	r	p-value	r	p-value	r	p-value
hfr mode 1	**-0.131**	**0.021**	**0.476**	**0.000**	0.109	0.056	-0.079	0.166
hfr mode 2	-0.016	0.777	**-0.140**	**0.014**	**0.213**	**0.000**	**0.127**	**0.025**
hfr mode 3	-0.066	0.245	**-0.127**	**0.025**	0.093	0.102	0.056	0.330
hfr mode 4	**-0.190**	**0.001**	-0.033	0.559	-0.064	0.260	-0.080	0.161
sst mode 1	**0.085**	**0.046**	**-0.349**	**0.000**	**0.185**	**0.000**	**0.173**	**0.000**
sst mode 2	-0.031	0.471	**-0.245**	**0.000**	-0.010	0.808	0.082	0.053
sst mode 3	-0.027	0.521	**0.183**	**0.000**	-0.020	0.641	-0.006	0.890
sst mode 4	0.022	0.602	**0.155**	**0.000**	0.015	0.731	**0.100**	**0.018**

4.5 San Francisco Bay Plume

4.5.1 Monthly climatology

The monthly climatology of the San Francisco Bay Plume—defined as the normalized water-leaving radiance at 555 nm ≥ 11 W m^{-2} μm^{-1} sr^{-1}—is shown in Figure 22. The plume is largest in the wintertime, reaching a maximum in January, and smallest from mid-summer to early fall, reaching a minimum in September. From January–September the plume progressively decreases in size with each coming month, and from October–December it progressively increases.

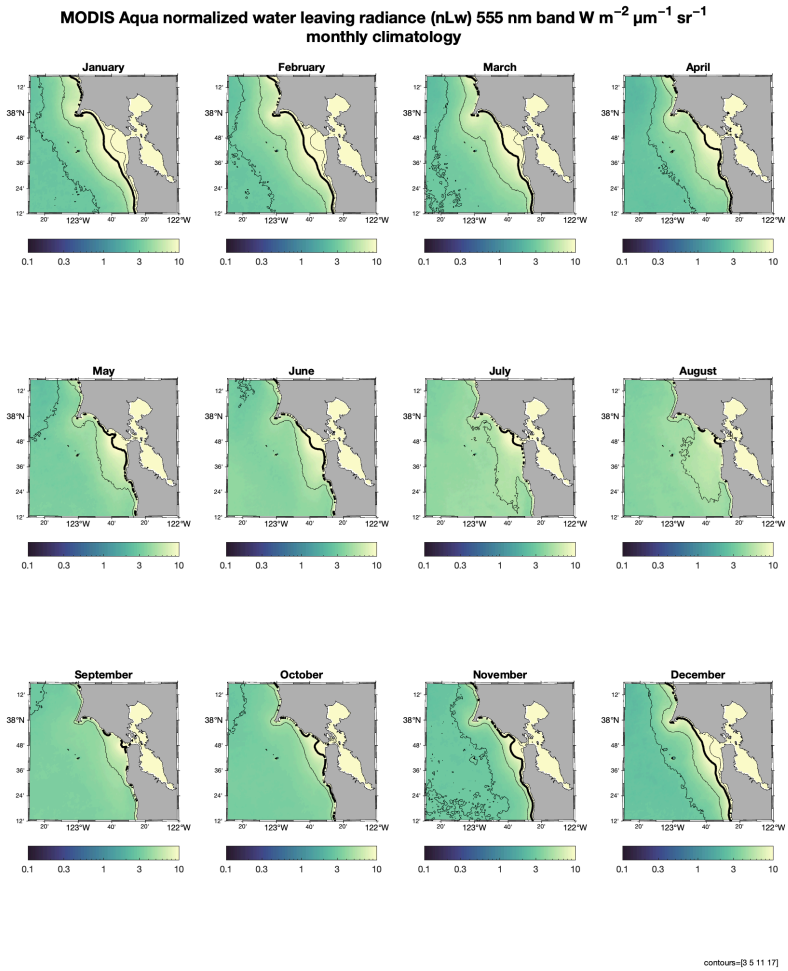

Figure 22. Normalized water-leaving radiance at the 555 nm band (nLw555) monthly climatology with units of W m^{-2} μm^{-1} sr^{-1}. Monthly means were calculated using the daily MODIS Aqua nLw555 product (2002-2021). Contours represent where nLw555 is 3, 5, 11, and 17 W m^{-2} μm^{-1} sr^{-1}. The thick contour represents the plume threshold of 11 W m^{-2} μm^{-1} sr^{-1}. Labeled color bars are located beneath each subplot.

4.5.2 Plume vs. chlorophyll anomalies

Scatter plots of the monthly and daily anomalies in chlorophyll against the SF Bay Plume are shown in Figure 23. A moderate positive correlation was found between the monthly chlorophyll anomalies and the plume, and a weak positive correlation was found between the daily chlorophyll anomalies and the plume. The correlation coefficient was statistically significant at the 5% level for both the monthly chlorophyll anomalies (H_0: r = 0; r = 0.33; p = 0.02) and the daily chlorophyll anomalies (H_0: r = 0; r = 0.29; p = 0.00). Therefore, the null hypothesis that no relationship exists between the monthly and daily chlorophyll anomalies and the San Francisco Bay Plume was rejected.

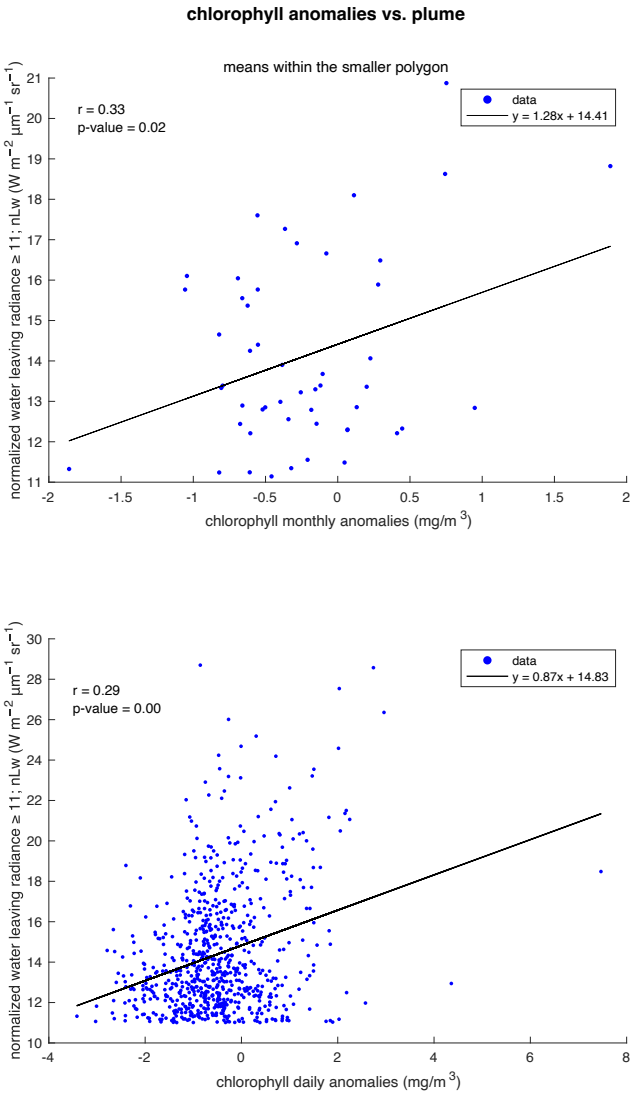

Figure 23. Scatter plots of the monthly (upper) and daily (lower) chlorophyll anomalies (mg/m^3) vs. nLw555 ≥ 11 W m^{-2} µm^{-1} sr^{-1}, defined as the San Francisco Bay Plume. A least squares regression line (or line of best fit) is overlain on each figure. The r value and p-value are displayed in the upper left side of each figure and a legend in their upper right. Chlorophyll anomalies were calculated using the daily OC-CCI product (1997-2021) and nLw555 was retrieved from the daily MODIS Aqua product (2002-2021).

5 Discussion

5.1 Overview: Study area

This paper focuses on data analysis of the Gulf of the Farallones. Located at the interface between coastal waters of the California Current System and potential interactions with San Francisco Bay, the Gulf is both unique and ecologically important. We focus mostly on characterizing means and variability from remotely sensed data within a small polygonal region extending from Jenner (38.4°N) at its northernmost point to near Año Nuevo Point at its southernmost point. Westward of the coast, it encompasses much of the continental shelf and at its most offshore point reaches the shelf break and slope seaward of the Farallon Islands (Fig. 1).

The bathymetry of the Gulf is unusual to rest of the U.S. west coast, due in part to its relatively wide shelf (Steger et al., 1998; Yen et al., 2004). In many places along the California coast, the continental shelf can be as narrow as 6-8 km, while in the vicinity of the Gulf it widens to approximately 50 km (Steger et al., 1998). An additional characteristic that makes the Gulf shelf unique is the direction with which it slopes. Much of the continental shelf off the coast of California slopes seaward—west or southwest—from the shoreline to the shelf break; however, the shelf in the Gulf slopes to the northwest, subparallel to the shoreline (Chin et al., 1997). Also distinctive topographically, the Gulf is located in the shadow of Pt. Reyes, resulting in retentive features (Largier, 2020; Vander Woude et al., 2006). All of these qualities have the ability to alter the circulation in our study region independent of the impacts of upwelling.

5.2 Seasonal cycle

Eastern boundary systems are well known to experience seasonal cycles of wind forcing that subsequently influence offshore Ekman transport, currents and sea surface temperature through upwelling, as well as chlorophyll through the transport and delivery of nutrients,

which support high rates of photosynthesis (García-Reyes & Largier, 2010; Henson & Thomas, 2007; Hickey, 1998; Largier, 2020; Thomas et al., 2004). The chlorophyll signal outside the Golden Gate in the Gulf of the Farallones is most prominent from April to August (Fig. 7), coincident with previously observed periods of maximum upwelling along the California coast (Hickey, 1998). Largier et al. (1993) identified the timing of an upwelling season, relaxation season, and storm season for an area that encompassed our study domain in its southern region and stretched up to Cape Blanco, Oregon (42.8°N) at its northern edge. Upwelling season was defined as the period from April–July, relaxation season as the period from August–November, and storm season as the period from December–March. Although the data analyzed in our study spans a much larger time period of more than 23 years (1997-2021), the findings of Largier et al. (1993) align with the monthly climatology shown in Figure 7, in which the chlorophyll signal is smallest from December–March, largest from April–July, and although still prominent, closer inshore from August–November. The transitions between seasons are most evident in March–April (spring transition), July–August (upwelling-relaxation), and November, just prior to the beginning of storm season.

Surface currents throughout our study domain are dominated by equatorward flow from March–June, particularly at the beginning of the upwelling season in April and May, while offshore flow dominates from October–January, particularly at the start of the storm season in December and January (Fig. 14). In July, August, and September, circulation over the slope is dominated by offshore flow, while equatorward flow dominates surface currents over the shelf. The transition from storm season to upwelling season is most evident in February, when mean surface currents begin to transition from offshore to equatorward flow.

Averaged over a nearly 20-year record of sea surface temperature, surface waters are warmest from August–October—particularly in September—coinciding with the relaxation season, and coolest in April and May due to a tongue of cool water that enters the Gulf from the area north of Pt. Reyes, coinciding with the upwelling season (Fig. 16). The entrance of

this cool water jet into the Gulf is likely a result of upwelled water north of Pt. Reyes that is advected by equatorward currents over the shelf (Kaplan & Largier, 2006; Steger et al., 2000).

5.3 Interannual variability

Poleward flow in our decadal monthly mean is only present along the coastline in the Gulf of the Farallones in the month of December. Gough et al. (2010) analyzed surface currents within the same study region estimated from September 1, 2006 through August 31, 2007 via HF Radar data obtained from three shore-based antennas. During the relaxation period of a single year—which they defined as October–December—significant poleward flow was observed over the slope, while equatorward flow dominated over the shelf through November. As surface waters begin to flow in the same direction as the California Undercurrent (CUC) in the fall and winter, otherwise known as the Davidson Current (Hickey, 1998), poleward flow is typically observed along the California coast both at the surface and at depth (Gough et al., 2010; Hickey, 1998). Ramp et al. (1997) found evidence of interruptions at depth to the CUC via meanders and mesoscale eddies that specifically occur off Monterey Bay in central California, sometimes resulting in complete reversals in flow transport farther north near the Gulf and Farallon Islands. In the present analysis, I analyzed mean monthly surface currents from 2012–2021 and found poleward flow to dominate in either or both December and January in 2012, 2014, 2016–2017, 2019, and 2021. However, in years 2013, 2015, 2018, and 2020, December and January months were characterized by largely equatorward and cross-shore flow that contributed to the climatological fields shown in Figure 14. This pattern may be evidence of a predictably recurrent interruption to the mean wintertime poleward flow of surface currents in the Gulf of the Farallones, occurring approximately every other year.

Originating near the central Gulf of Alaska and traveling south toward the coast, a large

region of anomalously high sea surface temperature—later described as 'the Blob'—was first observed in the winter of 2013–2014, but arrived along the coast of California in late 2014–early 2015, and persisted at least through the year 2016 (Barth et al., 2018). Also occurring in the year 2015–2016 was an El Niño event; however, compared with the impacts to the California Current System of previous extreme El Niño events (1982–1983 &1997–1998), the 2015–2016 event did not bring about anomalies that were similar in magnitude (Jacox et al., 2016). For example, cross-shore gradients were not as pronounced, the general temperature structure seemed to be unrelated to El Niño, wintertime deepening of the subsurface was much less dramatic, and surface winds did not fall into the window of what is expected during an El Niño (Jacox et al., 2016). As shown in Figure 24, the monthly anomaly in chlorophyll is exceptionally positive (upwards of +2.6 mg/m^3) in the year 2013 for March, June, September, and October, and exceptionally negative from September–October of 2014 (as low as -2.3 mg/m^3) and in July, August, and October of 2015 (-1.9 mg/m^3). The monthly SST anomalies

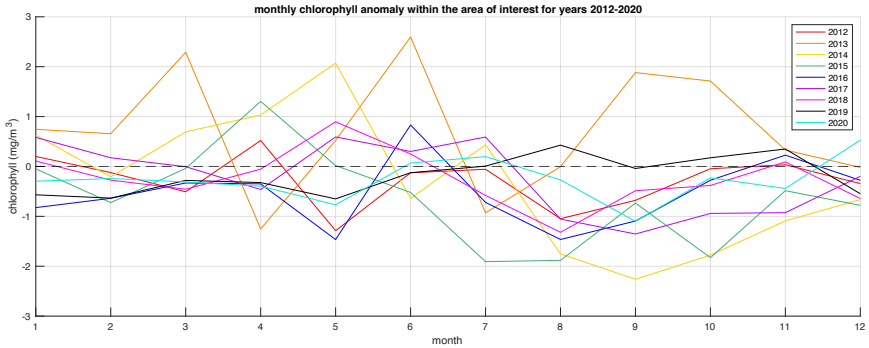

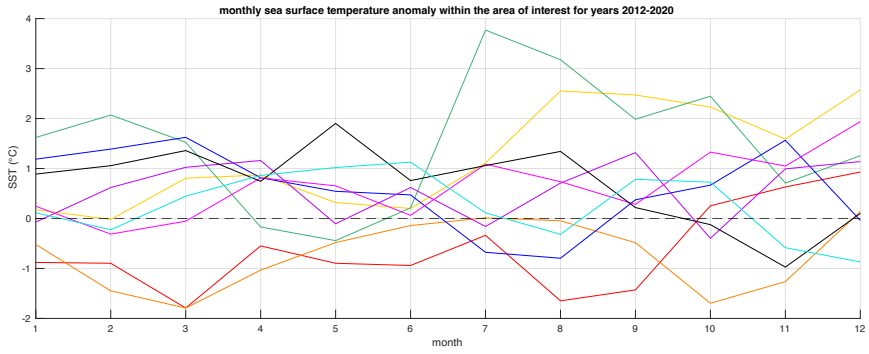

Figure 24. Time series of the monthly chlorophyll (mg/m^3) anomaly (upper) and SST (°C) anomaly (lower) within the area of interest for the years 2012-2020. Each year is plotted using a different color corresponding to the legend shown in the upper right corner of the upper panel. The line y = 0 is displayed as a black dashed line. Chlorophyll anomalies were calculated using the daily OC-CCI product (1997-2021) and SST anomalies were calculated using the 8-day NOAA MODIS Aqua product (2002-2022).

paint a similar—yet opposite—picture. For SST, monthly anomalies are exceptionally positive during August, September, October, and December of 2014 (upwards of +2.6°C), as well as February, July, August, September, and October of 2015 (+3.8°C). 2013 was anomalously negative for most of the year (as low as -1.8°C), with the exception of July and December, which are both close to the 20-year monthly mean. Figure 25 shows a significant negative correlation of moderate strength between anomalies in chlorophyll and anomalies in SST (r = -0.32; p-value = 0.00) over a nearly 20-year time period. It is reasonable to conclude that the extreme anomalies during 2014 and 2015 in both chlorophyll and SST observed in the Gulf of the Farallones are likely directly related to the occurrence of the 'warm blob'. Furthermore, any anomalies specific to 2015 are likely more related to the 2014–2015 'warm blob' than to the 2015–2016 El Niño.

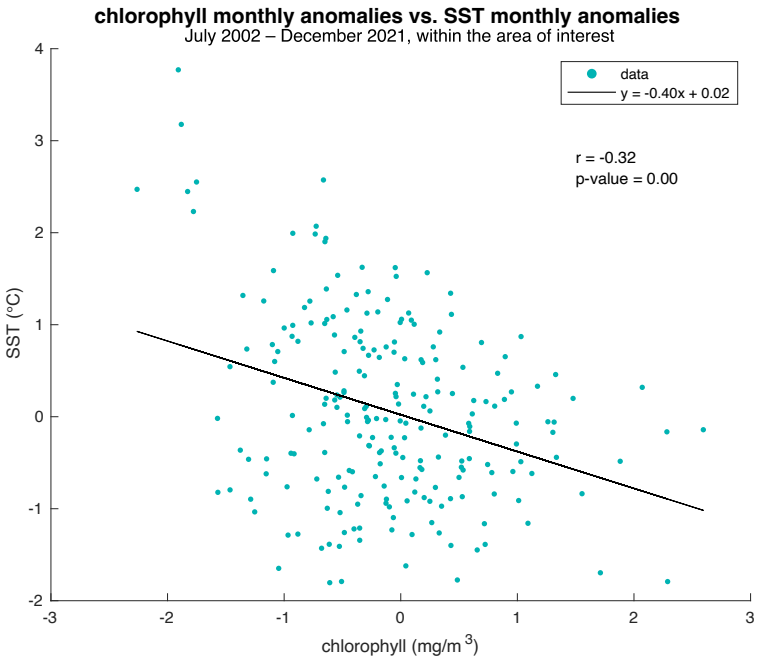

Figure 25. Scatter plot of the monthly chlorophyll (mg/m^3) anomalies vs. the monthly SST (°C) anomalies within the area of interest from July 2002-December 2021. A least squares regression line (or line of best fit) is overlain on the figure. The r value and p-value are displayed in the upper right and above that is a legend. Chlorophyll anomalies were calculated using the daily OC-CCI product (1997-2021) and SST anomalies were calculated using the 8-day NOAA MODIS Aqua product (2002-2022).

5.4 Short term variability

Our EOF analysis of chlorophyll (both linear and log-transformed), surface currents, and sea surface temperature overwhelmingly suggest that there is considerable variability of each

modal pattern described in this study throughout the duration of each month. The strongest significant correlation we found was between mode 1 of the HFR EOF—an alongshore surface current throughout the domain—and mode 2 of the log-transformed chlorophyll EOF—the north-south division—($r = 0.48$; $p = 0.00$; Table 1). This positive relationship of moderate strength suggests that when alongshore currents are traveling poleward, chlorophyll is enhanced in the region north of the Golden Gate and weakened in the region to its south, and when alongshore currents are traveling equatorward, the opposite is true of chlorophyll. This alongshore configuration of surface currents is expected during periods of downwelling; therefore, its relationship to the north-south chlorophyll pattern suggests a horizontal advection of chlorophyll in this region that is independent of upwelling. Kaplan et al. (2009) performed similar EOF analysis of HF Radar data in central California from 2006–2007, encompassing the nearshore region from Monterey Bay to just north of Bodega Bay, and also found an alongshore flow pattern to dominate mode 1 of their EOF, accounting for 31.4% of the variability in their data (about half of what mode 1 accounted for in both HFR EOFs in the present study; 2012–2022).

North of San Francisco Bay, the Columbia River Plume frequently experiences a bi-directional outflow in summer to early fall, in which plume waters propagate north and south of the river mouth simultaneously, and unidirectional in the winter, in which plume waters typically exclusively propagate northward (Hickey et al., 2005). They found this tendency to be due to changes in wind patterns and subsequent flow directions that shift on a monthly basis. Unlike the San Francisco Bay Plume which experiences a single spatial maximum in January (Fig. 22), the Colombia Plume experiences two maxima in its spatial volume, one in late spring and another in winter (Hickey et al., 2005). The amplitude time series of our EOF analysis shown in Figure 19 suggest that also unlike the Colombia River plume, the chlorophyll signal related to flow direction in the Gulf varies considerably throughout each month.

5.5 Influence of the SF Bay Plume

We investigated the direct influence of fresh water emerging from San Francisco Bay on chlorophyll within the Gulf with a remotely sensed data set collected at a particular wavelength that correlates with fresh water sources as a result of suspended sediment. The seasonal cycle of chlorophyll was nearly opposite to that of the plume (Figs. 7 & 22). As the chlorophyll signal decreases in size during the winter months, the plume increases in size, and as the chlorophyll signal increases in size during the spring and summer, the plume does the opposite. This suggests that the average patterns in chlorophyll and SF Bay Plume magnitude are actually caused by different mechanisms—likely upwelling and light availability for chlorophyll and wintertime rainfall for the plume. Despite this result for the monthly averages, a closer examination of anomalies yielded interesting findings (Fig. 23). Although we recognize that there is a lot of scatter, a significant positive correlation of moderate strength was found between monthly anomalies in chlorophyll and the magnitude of the plume ($r = 0.33$; $p = 0.02$), and a slightly weaker significant positive correlation was found when the daily anomalies in chlorophyll were used ($r = 0.29$; $p = 0.00$). This implies that at times when the chlorophyll signal is anomalously large, the plume is also large, and conversely, when the chlorophyll signal is anomalously small, the plume is also small. Therefore, although not obvious when looking at their monthly climatological fields, the plume does appear to possibly have an influence on anomalous events in the chlorophyll signal.

Using in situ data from the summers of 1999 and 2004, Hurst and Bruland (2008) argued that while the most apparent cause for the seasonality in the chlorophyll signal in the Gulf is coastal upwelling, Gulf of the Farallones primary production may in part result from continuous tidal fluxes of dissolved nutrients and bioactive trace metals from San Francisco Bay. Our analysis cannot resolve the impact of continuous tidal fluxes.

5.6 Challenges

The removal of frames that exceeded a set threshold for missing data points introduced a slight bias into the EOF analyses, particularly that of chlorophyll and SST (Fig. 26). HFR coverage, on the other hand, was excellent. Cloud cover severely obstructs the collection of satellite chlorophyll and SST, which are both in the visible and near infrared radiation (IR). As a result, the modal patterns shown in Figures 9, 10, 17, 18, and 20 may be biased toward periods of decreased cloud cover and increased chlorophyll concentrations, specifically in the months of July and August. That said, the biases are relatively minimal. Interestingly, July and August are also the months that separate the two peaks we observed in the bimodal time series of the monthly climatology of chlorophyll in the Gulf of the Farallones (Fig. 7). The chlorophyll plume at that time is still spatially prominent, but the magnitude of mean concentrations in the Gulf dip during those months.

For reference, the chlorophyll EOFs (linear and log-transformed) maintained 834 out of 1,120 frames, the SST EOF maintained 4,801 out of 6,560 frames, and the HFR EOF maintained 3,269 out of 3,720 frames. For the EOF correlation analysis between chlorophyll and surface currents, 310 out of 397 frames were maintained, and 557 out of 794 frames were maintained between chlorophyll and SST. The limited coverage of chlorophyll and SST required that we focus on a small area in the Gulf of the Farallones in order to minimize data filling, and this may have influenced the EOF patterns we calculated (Buell, 1979; Richman & Lamb, 1985). Specifically, EOF calculations over domains in which correlations remain positive throughout, as is the case here, are well known to yield so-called Buell patterns that reflect more the required orthogonality of the modes than the dominant patterns of variability. In such cases, modes can be combined and rotated to highlight particular non-orthogonal, but physically meaningful, patterns (e.g., using the varimax criterion of Kaiser, 1958). We are currently investigating these rotations further.

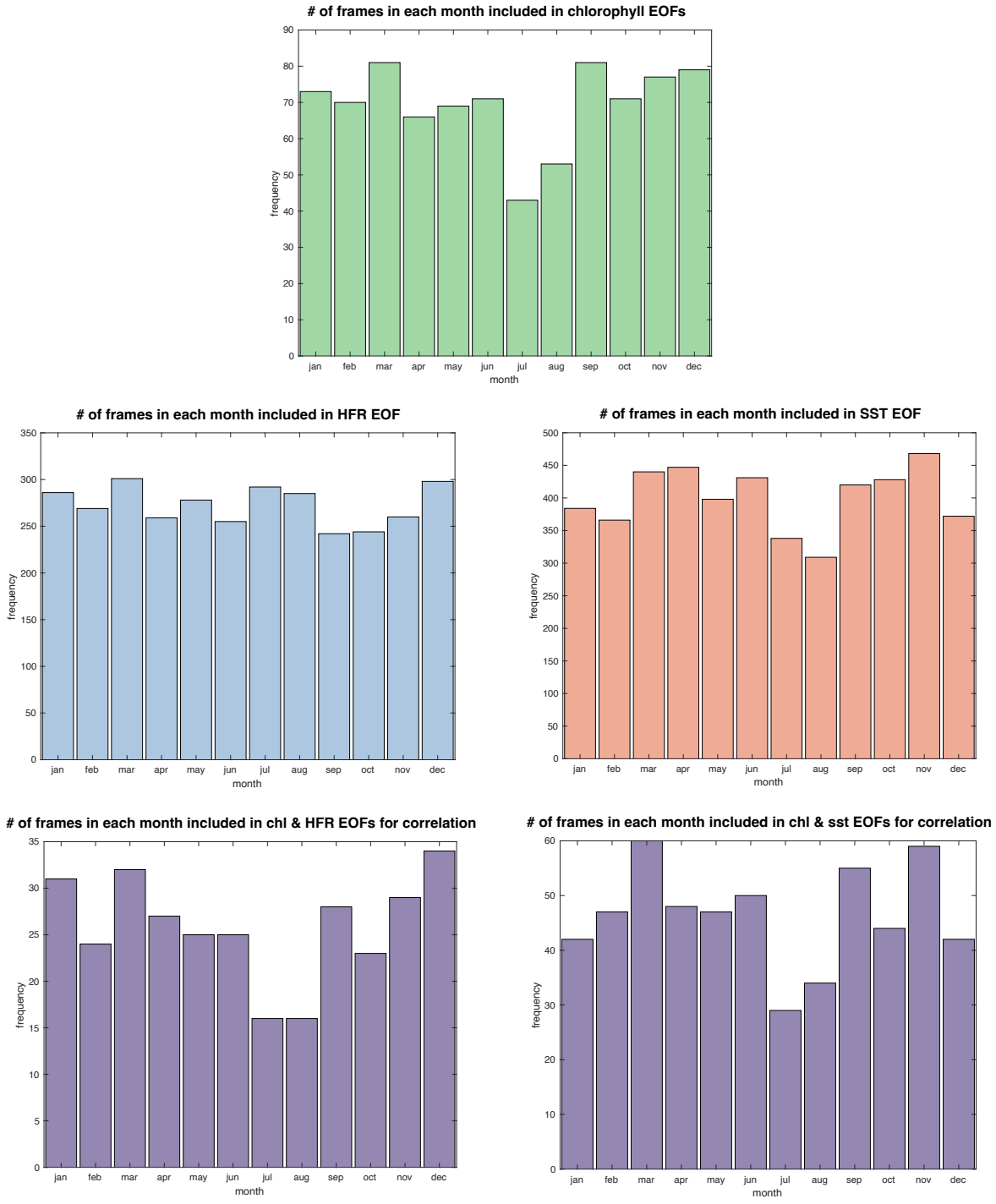

Figure 26. Histograms of the frequency of frames included for each month in the chlorophyll EOFs (upper, green), HFR EOF (mid-left, blue), SST EOF (mid-right, orange), chlorophyll & HFR EOFs for correlation analysis (lower left, purple), and chlorophyll & SST EOFs for correlation analysis (lower right, purple).

5.7 Conclusions

The 24-year (1997–2021) seasonal cycle of chlorophyll in the Gulf of the Farallones takes on a bimodal shape. The chlorophyll signal is smallest during the December–March storm season and largest during the April–July upwelling season; however, it is still prominent during the August–November relaxation season, just closer inshore.

A 10-year (2012–2022) monthly mean of surface currents reveals equatorward flow that dominates through most of the upwelling season, and offshore flow that dominates during the latter half of the relaxation season and most of the storm season. At the end of upwelling season and the first half of the relaxation season, offshore flow dominates over the slope and equatorward flow dominates over the shelf. Although only present along the coastline in the Gulf of the Farallones in the month of December from the climatological mean, poleward flow dominates the domain in either or both December and January approximately every other year from 2012–2021. This interannual variability in mean wintertime poleward flow in the Gulf may be evidence of a predictably recurrent interruption to the Davidson Current in this region.

A 20-year (2002–2022) seasonal cycle of sea surface temperature reveals surface waters to be coolest during the first half of upwelling season and warmest throughout the relaxation season. Anomalies in chlorophyll and anomalies in SST showed a significant, moderate, negative correlation over a 20-year time period in the Gulf of the Farallones ($p < 0.05$). Moreover, the extreme anomalies in both 2014 and 2015 are likely more related to the occurrence of the ‘warm blob’—which arrived along the California coast in 2014–2015—than they are to the 2015–2016 El Niño event.

Modal patterns shown in the EOF analysis of chlorophyll, surface currents, and SST vary considerably throughout each month, suggesting that the short-term variability of each mode shown occurs on a time scale of less than month. The most notable relationship between univariate EOFs is a significant, moderate, positive correlation between an alongshore current pattern and a north-south split in chlorophyll ($p < 0.05$), suggesting that

horizontal transport mechanisms—rather than vertical transport mechanisms (i.e., upwelling)—are impacting the distribution of chlorophyll in this region.

A 19-year (2002–2021) monthly climatology of the San Francisco Bay Plume, as represented by large magnitudes of normalized water-leaving radiance at 555 nm, shows a seasonal cycle opposite to that of chlorophyll; however, its magnitude is significantly, positively correlated to both monthly and daily anomalies in chlorophyll at the 5% level. This relationship provides insight into the potential impact that the San Francisco Bay Plume waters have on the ecosystem of the Gulf. Future studies should focus on further characterizing this relationship—such as, the impact of nutrient delivery into the Gulf via SF Bay and how ocean acidification and climate change have altered interactions between the Gulf ecosystem and SF Bay outflow through time—to ultimately aid conservation and management within these protected waters.

6 References

Banas, N. S., Hickey, B. M., MacCready, P., and Newton, J. A. 2004. Dynamics of Willapa Bay, Washington: A highly unsteady, partially mixed estuary. *Journal of Physical Oceanography, 34*: 2413-2427.

Barth, J. A., Fram, J. P., Dever, E. P., Risien, C. M. Wingard, C. E., Collier, R. W., and Kearney, T. D. 2018. Warm blobs, low-oxygen events, and an eclipse: The ocean observatories initiative endurance array captures them all. *Oceanography, 31*(1): 90-97.

Bonicelli, J., Moffat, C., Navarrete, S. A., Largier, J. L., and Tapia, F. J. 2014. Spatial differences in thermal structure and variability within a small bay: Interplay of diurnal winds and tides. *Continental Shelf Research, 88*: 72-80.

Brown, O. B. and Minnett, P. J. 1999. MODIS Infrared Sea Surface Temperature Algorithm, Version 2.0. *Algorithm Theoretical Basis Document, ATBD25*. University of Miami, Miami, FL. Under Contract Number NAS5-31361.

Buell, C. E. 1979. On the physical interpretation of empirical orthogonal functions. *Preprints of Sixth Conference on Probability and Statistics in Atmospheric Sciences,* American Meteorological Society: 112-117.

Chappell, A., Ells, A., and Mahoney, B. 2020. Recommendations and outcomes from the Sanctuary Advisory Council (2019) Symposium on connections between the San Francisco Bay and Greater Farallones National Marine Sanctuary. *NOAA Sea Grant, OAR (Oceanic and Atmospheric Research),* 1-14.

Chin, J. L., Karl, H. A., and Maher, N. M. 1997. Shallow subsurface geology of the continental shelf, Gulf of the Farallones, California, and its relationship to surficial seafloor characteristics. *Marine Geology, 137*: 251-269.

Cloern, J. E., Schraga, T. S., Nejad, E., Martin, C. 2020. Nutrient status of San Francisco Bay and its management implications. *Estuaries and Coasts, 43*: 1299-1317.

Colbert, D. and McManus, J. 2003. Nutrient biogeochemistry in an upwelling-influenced estuary of the Pacific Northwest (Tillamook Bay, Oregon, USA). *Estuaries, 26*(5): 1205-1219.

García-Reyes, M. and Largier, J. 2010. Observations of increased wind-driven coastal upwelling off central California. *Journal of Geophysical Research, 115*(C04011): 1-8.

Gough, M. K., Garfield, N., and McPhee-Shaw, E. 2010. An analysis of HF radar measured surface currents to determine tidal, wind-forced, and seasonal circulation in the Gulf of the Farallones, California, United States. *Journal of Geophysical Research, 115*(C04019): 1:19.

Greene, C. A., Thirumalai, K., Kearney, K. A., Delgado, J. M., Schwanghart, W., Wolfenbarger, N. S., Thyng, K. M., Gwyther, D. E., Gardner, A. S., and Blankenship, D. D. 2019. The Climate Toolbox for MATLAB. *Geochemistry, Geophysics, Geosystems, 20*(7): 3774-3781.

Henson, S. A. and Thomas, A. C. 2007. Interannual variability in timing and bloom initiation in the California Current System. *Journal of Geophysical Research, 112*(C08007): 1-12.

Hickey, B. M. 1998. Chapter 12. Coastal oceanography of western North America from the tip of Baja California to Vancouver Island, coastal segment (8,E). *The Sea, 11*: 345-393.

Hickey, B., Geier, S., Kachel, N., and MacFadyen, A. 2005. A bi-directional river plume: The Columbia in summer. *Continental Shelf Research, 25*: 1631-1656.

Horner-Devine, A. R., Hetland, R. D., and MacDonald, D. G. 2015. Mixing and transport in coastal river plumes. *Annual Review of Fluid Mechanics, 47*: 569-594.

Hurst, M. P. and Bruland, K. W. 2008. The effect of the San Francisco Bay plume on trace metal and nutrient distributions in the Gulf of the Farallones. *Geochimica et Cosmochimica Acta, 72*: 395-411.

Jacox, M. G., Hazen, E. L., Zaba, K. D., Rudnick, D. L., Edwards, C. A., Moore, A. M., and Bograd, S. J. 2016. Impacts of the 2015-2016 El Niño on the California Current System: Early assessment and comparison of past events. *Geophysical Research Letters, 43*, 7072-7080.

Kaiser, H. F. 1958. The varimax criterion for analytic rotation in factor analysis. *Psychometrika, 23*(3): 187-200.

Kaplan, D. M., Halle, C., Paduan, J., and Largier, J. L. 2009. Surface currents during anomalous upwelling seasons off central California. *Journal of Geophysical Research, 114*(C12026): 1-17.

Kaplan, D. M. and Largier, J. 2006. HF radar-derived origin and destination of surface waters off Bodega Bay, California. *Deep-Sea Research II*.

Kitchel, Z. J., Conrad, H. M., Selden, R. L., and Pinsky, M. L. 2022. The role of continental shelf bathymetry in shaping marine range shifts in the face of climate change. *Global Change Biology, 00*: 1-15.

Largier, J. L., Magnell, B. A., and Winant, C. D. 1993. Subtidal circulation over the northern California shelf. *Journal of Geophysical Research, 98*(C10): 18,147-18,179.

Largier, J. L. 2020. Upwelling bays: how coastal upwelling controls circulation, habitat, and productivity in bays. *Annual Review of Marine Science, 12*: 415-447.

Lynn, R. J. and Simpson, J. J. 1987. The California Current System: The seasonal variability of its physical characteristics. *Journal of Geophysical Research, 92*(C12): 12,947-12,966.

Lynn, R. J. and Simpson, J. J. 1990. The flow of the undercurrent over the continental borderland off southern California. *Journal of Geophysical Research, 95*(C8): 12,995-13,008.

MATLAB. 2021. 9.11.0.1873467 (R2021b) Update 3, The MathWorks, Inc., Natick, Massachusetts, United States.

Office of National Marine Sanctuaries. 2010. Gulf of the Farallones National Marine Sanctuary Condition Report 2010. *U.S. Department of Commerce, National Oceanic and Atmospheric Administration (NOAA), Office of National Marine Sanctuaries,* 1-97.

Otero, M. P. and Siegel, D. A. 2004. Spatial and temporal characteristics of sediment plumes and phytoplankton blooms in the Santa Barbara Channel. *Deep Sea Research II, 51*: 1129-1149.

Pitcher, G. C., Probyn, T. A., du Randt, A., Lucas, A. J., Bernard, S., Evers-King, H, Lamont, T., and Hutchings, L. 2014. Dynamics of oxygen depletion in the nearshore of a coastal embayment of the southern Benguela upwelling system. *Journal of Geophysical Research: Oceans, 119*: 2183-2200.

Raimont, M. and Cloern, J. E. 2017. Estuary-ocean connectivity: fast physics, slow biology. *Global Change Biology, 23*: 2345-2357.

Ramp, S. R., Rosenfeld, L. K., Tisch, T. D., and Hicks, M. R. 1997. Moored observations of the current and temperature structure over the continental slope off central California. 1. A basic description of the variability. *Journal of Geophysical Research, 102*(C10): 22,877-22,902.

Richman, M. B. and Lamb, P. J. 1985. Climatic pattern analysis of three- and seven-day summer rainfall in the central United States: Some methodological consideration and a regionalization. *Journal of Climate and Applied Meteorology, 24*: 1325-1343.

Ryan, J. P., Fischer, A. M., Kudela, R. M., McManus, M. A., Myers, J. S., Paduan, J. D., Ruhsam, C. M., Woodson, C. B., and Zhang, Y. 2010. Recurrent frontal slicks of a coastal ocean upwelling shadow. *Journal of Geophysical Research, 115*(C12070): 1-15.

Sathyendranath, S., Brewin, R. J. W., Brockmann, C., Brotas, V., Calton, B., Chuprin, A., Cipollini, P., Couto, A. B., Dingle, J., Doerffer, R., Donlon, C., Dowell, M., Farman, A., Grant, M., Groom, S., Horseman, A., Jackson, T., Krasemann, H., Lavender, S., Martinez-Vicente, V., Mazeran, C., Mélin, F., Moore, T. S., Müller, D., Regner, P., Roy, S., Steele, C. J., Steinmetz, F., Swinton, J., Taberner, M., Thompson, A., Valente, A., Zühlke, M., Brando, V. E., Feng, H., Feldman, G., Franz, B. A., Frouin, R., Gould, Jr., R. W., Hooker, S. B., Kahru, M., Kratzer, S., Mitchell, B. G., Muller-Karger, F., Sosik, H. M., Voss, K. J., Werdell, J., and Platt, T. 2019. An ocean-colour time series for use in climate studies: the experience of the Ocean-Colour Climate Change Initiative (OC-CCI). *Sensors*: 19, 4285.

Sathyendranath, S., Jackson, T., Brockmann, C., Brotas, V., Calton, B., Chuprin, A., Clements, O., Cipollini, P., Danne, O., Dingle, J., Donlon, C., Grant, M., Groom, S., Krasemann, H., Lavender, S., Mazeran, C., Mélin, F., Müller, D., Steinmetz, F., Valente, A., Zühlke, M., Feldman, G., Franz, B., Frouin, R., Werdell, J., Platt, T. 2021. ESA Ocean Colour Climate Change Initiative (Ocean_Colour_cci): Version 5.0 Data. *NERC EDS Centre for Environmental Data Analysis,* 19 May 2021.

Souto, C., Gilcoto, M., Fariña-Busto, L., and Pérez, F. F. 2003. Modeling the residual circulation of a coastal embayment affected by wind-driven upwelling: Circulation of the Ría de Vigo (NW Spain), *Journal of Geophysical Research, 108*(C11): 3340-3358.

Steger, J. M., Collins, C. A., Schwing, F. B., Noble, M., Garfield, N., and Steiner, M. T. 1998. An empirical model of the tidal currents in the Gulf of the Farallones. *Deep-Sea Research II, 45*: 1471-1505

Steger, J. M., Schwing, F. B., Collins, C. A., Rosenfeld, L. K., Garfield, N., and Gezgin, E. 2000. The circulation and water masses in the Gulf of the Farallones. *Deep-Sea Research II, 47*: 907-946.

Terrill, E. *et al.* 2006. Data Management and Real-time Distribution in the HF-Radar National Network. *Proceedings of the MTS/IEEE Oceans 2006 Conference,* Boston MA, September 2006.

Tezak, S., Esri ArcGIS 10.5, and NOAA National Centers for Environmental Information (NCEI). 2017. Greater Farallones National Marine Sanctuary. Retrieved June 25, 2022, from https://farallones.noaa.gov/gallery/maps.html

Thomas, A. C., Strub, P. T., Carr, M. E., and Weatherbee, R. 2004. Comparisons of chlorophyll variability between the four major global eastern boundary systems. *International Journal of Remote Sensing, 25*(7-8): 1443-1447.

Trautman, N. and Walter, R. K. 2021. Seasonal variability of upwelling and downwelling surface current patterns in a small coastal embayment. *Continental Shelf Research, 226*(104490): 1-12.

Vander Woude, A. J., Largier, J. L., and Kudela, R. M. 2006. Nearshore retention of upwelled waters north and south of Point Reyes (northern California)—Patterns of surface temperature and chlorophyll observed in CoOP WEST. *Deep-Sea Research II 53*: 2985-2998.

Walter, R. K., Armenta, K. J., Shearer, B., Robbins, I., Steinbeck, J. 2018. Coastal upwelling seasonality and variability of temperature and chlorophyll in a small coastal embayment, *Continental Shelf Research, 154*: 9-18.

Wang, M., Son, S., and Shi, W. 2009. Evaluation of MODIS SWIR and NIR-SWIR atmospheric correction algorithms using SeaBASS data. *Remote Sensing of Environment, 113*: 635-644.

Yasui, T., Abe, H., Hirawake, T., Sasaki, K., and Wakita, M. 2022. Seasonal pathways of the Tsugaru Warm Current revealed by high-frequency ocean radars. *Journal of Oceanography, 78*: 103-119.

Yen, P. P. W., Sydeman, W. J., and Hyrenbach, K. D. 2004. Marine bird and cetacean associations with bathymetric habitats and shallow-water topographies: implications for trophic transfer and conservation. *Journal of Marine Systems, 50*: 79-99.